Color screening and regeneration of bottomonia in high-energy heavy-ion collisions

X. Du,[1] M. He,[2] and R. Rapp[1]

[1] *Cyclotron Institute and Department of Physics and Astronomy, Texas A&M University, College Station, TX 77843-3366, USA*

[2] *Department of Applied Physics, Nanjing University of Science and Technology, Nanjing 210094, China*

(Dated: March 12, 2022)

The production of ground-state and excited bottomonia in ultrarelativistic heavy-ion collisions is investigated within a kinetic-rate equation approach including regeneration. We augment our previous calculations by an improved treatment of medium effects, with temperature-dependent binding energies and pertinent reaction rates, B-meson resonance states in the equilibrium limit near the hadronization temperature, and a lattice-QCD based equation of state for the bulk medium. In addition to the centrality dependence of the bottomonium yields we compute their transverse-momentum (p_T) spectra and elliptic flow with momentum-dependent reaction rates and a regeneration component based on b-quark spectra from a nonperturbative transport model of heavy-quark diffusion. The latter has noticeable consequences for the shape of the bottomonium p_T spectra. We quantify how uncertainties in the various modeling components affect the predictions for observables. Based on this we argue that the $\Upsilon(1S)$ suppression is a promising observable for mapping out the in-medium properties of the QCD force, while $\Upsilon(2S)$ production can help to quantify the role of regeneration from partially thermalized b quarks.

I. INTRODUCTION

Heavy quarkonia have long been recognized as a promising probe of the modifications of the fundamental QCD force in hot and dense matter. In vacuum, the potential between a heavy quark and antiquark is well established in terms of a short-range Coulombic part and a long-range linear "confining" part, which allows for a robust phenomenology of the charmonium and bottomonium bound-state spectra. This can serve as a controlled starting point for their in-medium spectroscopy [1–4]. Measurements of quarkonia in ultrarelativistic heavy-ion collisions (URHICs) have much progressed over the last decade, mostly carried out via the dilepton decay channel of the vector states J/ψ, ψ' and the $\Upsilon(1S, 2S, 3S)$ family, cf. Refs. [5, 6] for recent overviews. While the observed invariant-mass spectrum does not include significant information about their in-medium properties (since the vast majority of the dilepton decays occurs long after the fireball has frozen out), systematic studies of quarkonium production yields as a function of collision centrality, energy ($\sqrt{s}$), and transverse momentum (p_T) have provided a rich source of information on how their properties are affected in the presence of a hot QCD medium.

For charmonia, an interplay of thermal suppression and regeneration reactions throughout the evolution of the fireball formed in nuclear collisions turned out to provide a suitable framework to describe the observed production patterns from CERN Super Proton Synchrotron (SPS) energy (0.017 TeV) [7], via BNL Relativistic Heavy Ion Collider (RHIC) energy (0.039-0.2 TeV) [8, 9], to CERN Large Hadron Collider (LHC) energy (2.76 TeV) [10], see also [11–18]. In particular, the relative enhancement of J/ψ yields when going from RHIC to the LHC was anticipated as a consequence of regeneration processes which intensify in the presence of larger charm-quark densities in the system. This interpretation was corroborated by the measured p_T spectra, which confirmed the prediction that the regeneration yields are concentrated at low $p_T \lesssim m_\Psi$ [10].

For bottomonia, the role of regeneration processes is less obvious. In Pb-Pb($\sqrt{s}$=2.76 TeV) collisions at the LHC, the CMS Collaboration [19] reported a "sequential suppression" of bottomonia, characterized by an increasing level of suppression for $\Upsilon(1S)$, $\Upsilon(2S)$ and $\Upsilon(3S)$ states, following their ordering in vacuum binding energy. These data, along with the inclusive Υ data from the STAR and PHENIX Collaborations in Au-Au($\sqrt{s}$=0.2 TeV) and U-U($\sqrt{s}$=0.193 TeV) collisions at RHIC [20–22], can indeed be reasonably well described by models which do not include regeneration contributions [23–25]. This is more challenging for recent ALICE data at forward rapidity, which exhibit stronger suppression [26] than at mid-rapidity, even though a less dense medium is expected to form at forward rapidity. Cold-nuclear-matter (CNM) effects may play a role in this observation, as shadowing effects could be more pronounced at forward rapidity. Since the typical ratio of Υ relative to total $b\bar{b}$ production is only about 0.1% in elementary pp collisions (compared to $\sim$1% for charmonium to total $c\bar{c}$ production), even small regeneration yields in URHICs may give a significant contribution to the observed Υ production [27]. In Ref. [28], this was quantitatively investigated in a kinetic-rate-equation framework. On the one hand, it was found that regeneration contributions in 2.76 TeV Pb-Pb collisions are moderate for the $\Upsilon(1S)$ state, at a $\sim$20% level of the total yield in central Pb-Pb collisions (including feeddown from higher states). On the other hand, with a strong suppression of primordially produced $\Upsilon(2S)$ states [down to $\lesssim$5% in central Pb-Pb(2.76 TeV] collisions), the regeneration yield emerged as the dominant source for semi-central and central collisions. The calculated centrality dependence of the nuclear modification factors for both $\Upsilon(1S)$

and $\Upsilon(2S)$ turned out to be in approximate agreement with the CMS data, provided a so-called "strong-binding scenario" (SBS) was employed, where the bottomonium binding energies were assumed to be at their vacuum values. This was qualitatively motivated by theoretical scenarios with a heavy-quark (HQ) potential taken as the internal energy computed in lattice QCD (lQCD) [29]. Similar findings where also reported in other transport approaches [23, 30]. The magnitude of the regeneration contribution for the $\Upsilon(1S)$, however, does not suffice to account for the stronger suppression of the ALICE data at forward rapidity, relative to mid-rapidity. Clearly, the decomposition into primordial and regenerated components requires further studies. In the meantime, the CMS Collaboration has released p_T spectra for both $\Upsilon(1S)$ and $\Upsilon(2S)$ [31], providing an excellent opportunity for additional tests and tuning of model calculations [23].

In the present work we extend our previous calculations of bottomonium kinetics in the fireballs of URHICs in several respects. For a more realistic treatment of the in-medium properties of bottomonia we implement in-medium binding energies as extracted from microscopic T-matrix calculations [29]. These affect both the inelastic reaction rates and the equilibrium limit of bottomonium abundances which figure in the regeneration reactions. The space-time evolution of the fireball is updated by using a lQCD-based equation of state (EoS) [32]. We compute the production yields of $\Upsilon(1S, 2S, 3S)$ states as well as their p_T spectra and the elliptic flow (v_2) based on 3-momentum dependent dissociation rates and b-quark spectra for regeneration processes which are taken from nonperturbative transport simulations (which give a fair description of open-bottom observables at the LHC [33]). In contrast to c quarks, b-quark spectra are not expected to reach near thermalization at the RHIC and the LHC, which has a significant impact on the p_T dependence of bottomonium regeneration. Since primordial Υ states are not expected to acquire a large v_2, their measured total v_2 may provide a greater sensitivity to regeneration processes than the inclusive yields or even p_T spectra. We also calculate bottomonium observables for 5.02 TeV Pb-Pb collisions as recently measured at the LHC.

Our paper is organized as follows. In Sec. II we briefly recall the basic ingredients of our kinetic-rate-equation approach, with emphasis on its improvements over previous work [28]. In particular, we scrutinize various mechanisms in the dissociation rates in the presence of in-medium effects on the bottomonium binding energies, improve the Υ equilibrium limits by accounting for B-meson resonance states near T_c (Sec. II A), and replace a massless-gas EoS in the fireball evolution with a parametrization from lQCD (Sec. II B); we also discuss how we calculate Y p_T spectra and their elliptic flow (Sec. II C), and the open-bottom and bottomonium input cross sections needed for phenomenology (Sec. II D). In Sec. III we start the systematic comparison of our updated results to available data with Au-Au and U-U systems at the RHIC including both centrality (Sec. III A) and p_T dependencies (Sec. III B). In Sec. IV we turn to Pb-Pb(2.76 TeV) collisions at the LHC, studying centrality and rapidity dependencies for both the previously employed SBS (Sec. IV A) and our updated approach (Sec. IV B), conducting a sensitivity study of model parameters (Sec. IV C), and then turning to p_T spectra (Sec. IV D) and v_2 (Sec. IV E). In Sec. V we provide predictions for Pb-Pb(5.02 TeV) collisions, again contrasting the previous SBS (Sec. V A) with the updated approach (Sec. V B), including comparisons to recently available data for $\Upsilon(1S)$, $\Upsilon(2S)$ and $\Upsilon(3S)$ states. In Sec. VI we summarize our results in terms of an excitation function of the nuclear modification factor for both $\Upsilon(1S)$ and $\Upsilon(2S)$ in comparison to data from the RHIC and the LHC. In Sec. VII we summarize and conclude.

II. BOTTOMONIUM TRANSPORT IN MEDIUM

In this work we utilize a kinetic-rate equation [11] as our simulation tool for the time evolution of bottomonium abundances in URHICs [27, 28]. We first introduce its basic framework and main transport parameters – reaction rate and equilibrium limit – in Sec. II A, review the bulk medium evolution in Sec. II B, describe the calculation of the p_T spectra and elliptic flow of bottomonia in Sec. II C, and summarize our input cross sections to the rate equation for open bottom and bottomonia as constrained by pp data in Sec. II D.

A. Kinetic rate equation and transport coefficients

The rate equation for a given Y state is characterized by loss and gain terms as

$$\frac{\mathrm{d}N_Y(\tau)}{\mathrm{d}\tau} = -\Gamma_Y(T(\tau))\left[N_Y(\tau) - N_Y^{\mathrm{eq}}(T(\tau))\right] \ , \qquad (1)$$

where the two transport coefficients are the inelastic reaction rate, Γ_Y, and the equilibrium limit, N_Y^{eq}. We include the bottomonium states $Y = \Upsilon(1S), \Upsilon(2S), \Upsilon(3S), \chi_b(1P)$ and $\chi_b(2P)$, where we combine the three states $\chi_{b0,1,2}$ into a single one, as their vacuum mass splittings are within ∼60 MeV. Since the vacuum binding energies of most of these states, commonly defined as $E_B^Y = 2m_B - m_Y$, are significantly larger than the pseudo-critical QCD transition temperature, T_{pc}, we neglect inelastic reactions in the hadronic phase (they may become important for $E_B^Y \lesssim T_{\mathrm{pc}}$, *i.e.*, for the $\Upsilon(3S)$, and $\chi_b(2P)$, similarly to the ψ' [34]) and focus on the kinetics in the quark-gluon plasma (QGP) down to a (pseudo-) critical temperature of T_{pc}=170 MeV.

1. *In-medium binding energies and dissociation rates*

The nature of the quarkonium dissociation rate in the QGP depends on the interplay of bound-state scales

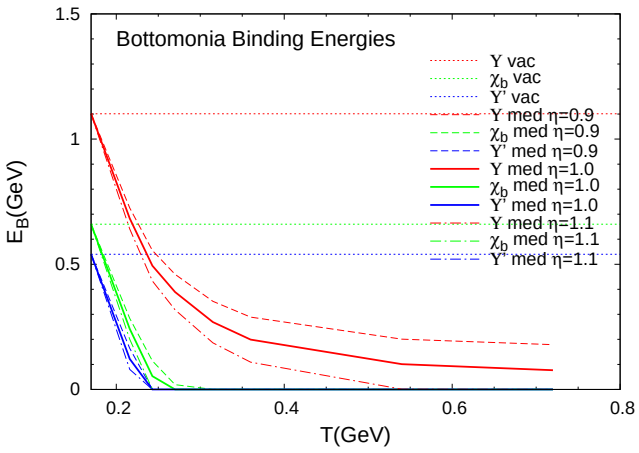

FIG. 1: Bottomonium binding energies for the SBS (vacuum E_B's, dotted lines) [28] and T-matrix binding scenarios (TBS) with baseline value [29] η=1.0 (solid lines), and a 10% smaller (η=0.9, dashed lines) or larger (η=1.1, dash-dotted lines) reduction in $\Delta E_B(T)$; cf. Eq. (3). The red, green, and blue lines are for $\Upsilon(1S)$, χ_b, and $\Upsilon(2S)$ states, respectively.

(*e.g.*, size and binding energy) and medium scales (*e.g.*, screening length (inverse Debye mass) and temperature) [27, 35, 36]. Our starting point is different scenarios for the in-medium binding energies, $E_B^Y(T)$, of the various bottomonium states. One may consider this as fundamental information that one would like to extract from the experimental data. This also includes the "melting" temperatures at which the states cease to exist, which generally do not coincide with a vanishing binding energy due to finite dissociation widths. However, the latter already affect the yields at temperatures (well) below the melting temperature, while the binding energies affect the dissociation mechanisms. In previous work [27, 28], the binding energies were bracketed by a strong-binding scenario (SBS), where the vacuum binding was simply assumed at all temperatures, and a weak-binding scenario (WBS), which was based on a screened Cornell potential [37] with a perturbative screening mass, $m_D \sim gT$ (see Fig. 3 in Ref. [27] or Fig. 1 in Ref. [28]). These scenarios were coupled with appropriate dissociation mechanisms, *i.e.*, gluo-dissociation ($g + Y \to b + \bar{b}$) for the SBS and quasifree dissociation ($p + Y \to b + \bar{b} + p$ with $p = q, \bar{q}, g$) for the WBS.

In the present work we instead adopt in-medium binding energies predicted by thermodynamic T-matrix calculations [29] using internal-energy potentials, $U_{\bar{Q}Q}$, from lQCD. This choice for the underlying potential is motivated by a better agreement with quarkonium correlators and charmonium phenomenology [13] compared to more weakly coupled scenarios (such as the free energy, $F_{\bar{Q}Q}$), and also by yielding a much smaller (*i.e.*, more strongly coupled) heavy-quark diffusion coefficient which is preferred by open heavy-flavor phenomenology [33]. More rigorous determinations of the in-medium potential are underway [38] and will be investigated in future work.

We denote the T-matrix binding scenario by TBS, and replot the temperature-dependent ground state binding energy by the red solid line in Fig. 1, as extracted from Fig. 27 left in Ref. [29]. We implement this together with the assumption of Y bound-state masses fixed at their vacuum values. This allows us to extract the in-medium b-quark mass from the relation

$$m_{\Upsilon(1S)} = 2m_b(T) - E_B^{\Upsilon(1S)}(T) \ , \tag{2}$$

and subsequently use this expression to infer the binding energies, $E_B^Y(T)$, of the excited states, which are also shown in Fig. 1. The use of internal energies from different lQCD computations induces uncertainties of a few tens of percent in the T-matrix calculations of $E_B^{\Upsilon(1S)}(T)$. To account for this, we will also allow for two scenarios where the in-medium reduction of the $\Upsilon(1S)$ binding energy, $\Delta E_B(T) = E_B^{\rm vac} - E_B(T)$, is decreased (increased) by 10%, i.e.,

$$E_B^\eta(T) \equiv E_B^{\rm vac} - \eta \Delta E_B(T) \tag{3}$$

with η=0.9 (η=1.1). This scenario is shown by the dashed (dash-dotted) lines in Fig. 1. In principle, one could consider η as a parameter to be extracted from a best fit to data. It turns out that the baseline TBS (η=1.0) transitions from the SBS close to $T_{\rm pc}$ to the WBS at temperatures above $T \simeq 350\,$MeV, where the binding energies of the excited states have vanished and the ground-state binding has dropped to about 200 MeV.

Next we turn to the bottomonium dissociation rates, starting with gluo-dissociation for $Y + g \to b\bar{b}$ given by [39]

$$\Gamma_Y^{\rm gd}(p_\Upsilon, T) = \int \frac{{\rm d}^3 p_g}{(2\pi)^3} d_g f_g(\omega_g, T) v_{\rm rel} \sigma_{Yg\to b\bar{b}}(s) \ . \tag{4}$$

Here, $f_g(\omega_g, T) = (\exp\left(\frac{\omega_g}{T}\right) - 1)^{-1}$ is the Bose distribution of gluons (with degeneracy d_g=16), $s = (p^{(4)} + p_g^{(4)})^2$, and

$$v_{\rm rel} = \frac{\sqrt{(p_1^{(4)} \cdot p_2^{(4)})^2 - m_1^2 m_2^2}}{\omega_1 \omega_2} \tag{5}$$

is the relative velocity of incoming particles. The gluo-dissociation cross sections for the different Y states are detailed in Appendix A. These rates have been utilized within the SBS in a heat bath of massless partons in Ref. [28] and are reproduced in the upper panel of Fig. 2. They are quite large, especially for the excited states, and were found to be compatible with the strong suppression of the $\Upsilon(2S)$ observed at the LHC. However, massless partons overestimate the EoS at given temperature, especially near $T_{\rm pc}$. Here we implement thermal gluon masses, $m_g = \sqrt{1/2(1 + N_f/6)}gT$, which suppress the rates not only for low temperatures (where $m_g < E_B$), but even more so once the gluon mass becomes comparable to the binding energy, For example, at T=300 MeV,

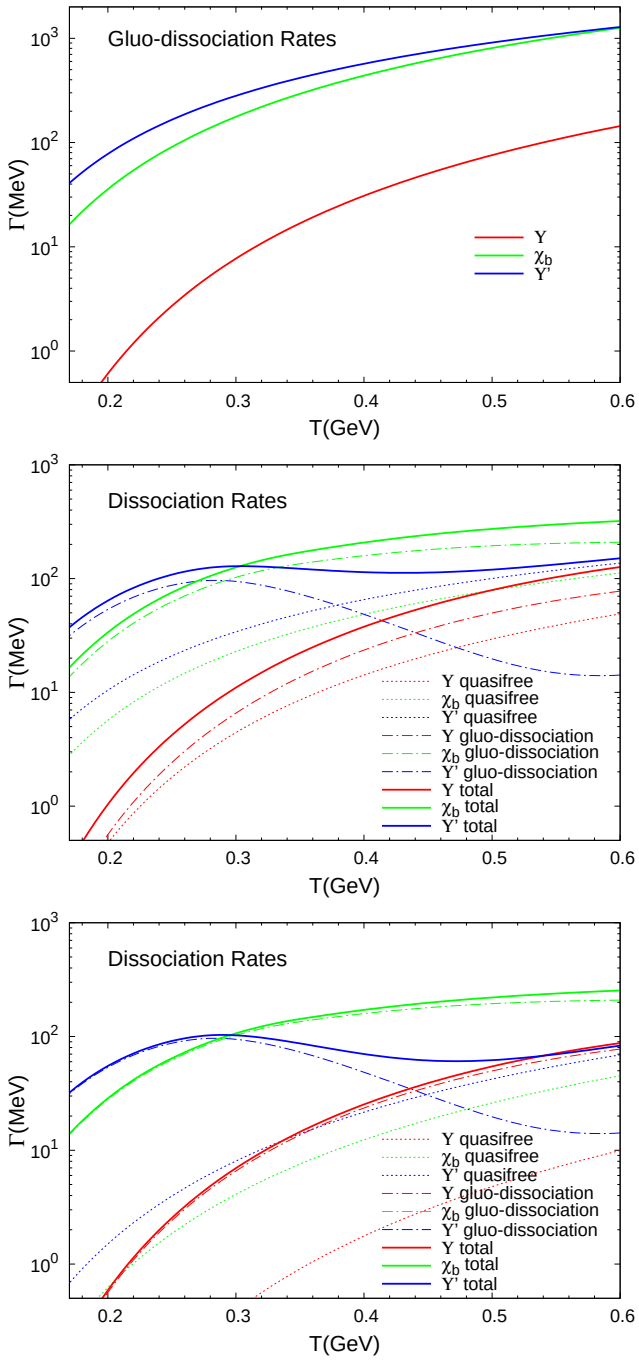

FIG. 2: Bottomonium dissociation rates in QGP for the SBS using gluo-dissociation with massless (upper panel) or massive gluons (dash-dotted lines in the middle and lower panel). The middle and lower panels also show the rates from inelastic "quasifree" scattering off massive quarks and gluons (dotted lines) without (middle panel) and with (lower panel) interference corrections, and their sum with massive gluo-dissociation rates (solid lines). All rates are evaluated at zero Y 3-momentum with a strong coupling constant of g=2.0.

the rates for the excited states are suppressed by around a factor of 2; see the dash-dotted lines in the middle (or lower) panel of Fig. 2.

In addition to gluo-dissociation, next-to-leading order inelastic parton scattering, $p + Y \to b + \bar{b} + p$ with $p = q, \bar{q}, g$, can suppress (or regenerate) Y bound states. The pertinent rate reads

$$\Gamma_Y^{\rm qf}(p,T) = \sum_p \int \frac{{\rm d}^3 p_p}{(2\pi)^3} d_p f_p(\omega_p,T) v_{\rm rel} \sigma_{Yp\to b\bar{b}p}(s) \ , \quad (6)$$

where f_p is the Fermi or Bose distribution for p=q,$\bar{q}$ or g. In previous work we have treated inelastic parton dissociation in "quasifree" (qf) approximation, applicable for weakly bound states, where the recoil of the spectator heavy quark or antiquark is neglected while conserving 4-momentum [35]. For binding energies comparable to, or larger than, the temperature sizable corrections are expected due to interference effects between the parton scattering off the heavy quark and antiquark [40, 41]. In particular, in the limit of small bound-state size, $r \to 0$, the width vanishes since the colored medium parton does not resolve the color-neutral Y configuration anymore. These corrections amount to an interference factor $(1-{\rm e}^{i\vec{q}\cdot\vec{r}})$ in the expression for the width, where $\vec{q}$ is the 3-momentum of the exchanged gluon. We implement the interference factor into the previously used quasifree width expression with the identification $\vec{q}^{\,2} \simeq -t$. The resulting Y widths for inelastic scattering off massive partons without and with interference correction are shown by the dotted lines in the middle and lower panels of Fig. 2, respectively. As expected, for the SBS the interference effects give large corrections, suppressing the rates by typically a factor of around 5 (more/less at low/high temperature). The massive quasifree rates are generally well below the massive gluo-dissociation rates, except for the $Y(2S)$ for $T \gtrsim 450$ MeV.

Our final scenario implements in-medium binding energies based on T-matrix calculations (TBS) of Ref. [29]. The reduced binding energies entail a substantial increase of the quasifree rates over the SBS, especially for the $\Upsilon(1S)$. Within the TBS, the latter shows significant sensitivity to the in-medium binding energy. For example, at T=350 MeV, when going from the η=1.0 baseline scenario to $\eta = 0.9$ ($\eta = 1.1$), where the binding energy varies from ∼200 MeV in the former to ∼300 MeV (∼100 MeV) in the latter, the width decreases (increases) by about 25% (50%), from 80 to 60 MeV (120 MeV), and similarly at other temperatures, see Fig. 3. Variations in the already small binding energy of the excited states have rather little impact on their rates. Furthermore, the gluo-dissociation mechanism in the TBS is only relevant in a small temperature window above $T_{\rm pc}$.

We note that the Bose-enhancement/Pauli-blocking factors, $(1\pm f_p)$, of the outgoing light partons in the quasifree reaction rate, Eq. (6), have been neglected. Their effect is an increase/decrease of the rate for outgoing gluons/quarks by less than 10%, respectively, which essentially cancel each other in the sum; see Fig. 4.

In Figs. 5, 6 and 7 we display the 3-momentum (p) dependence of the rates for the binding energy scenar-

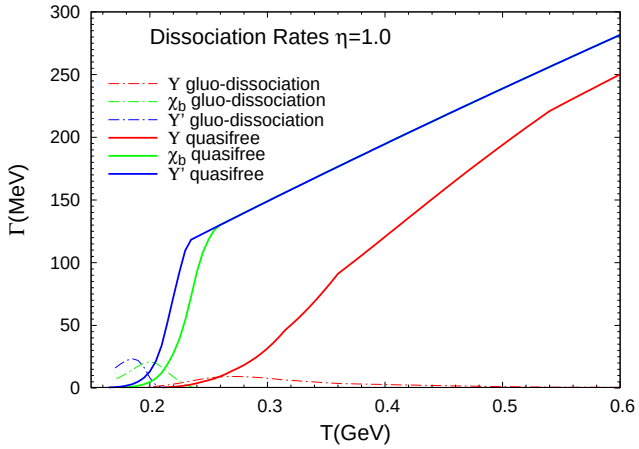

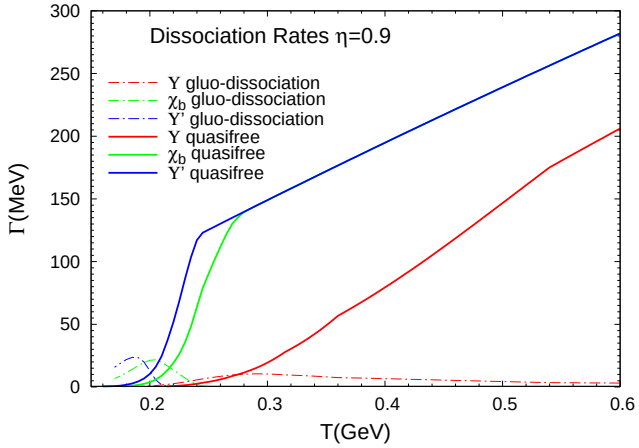

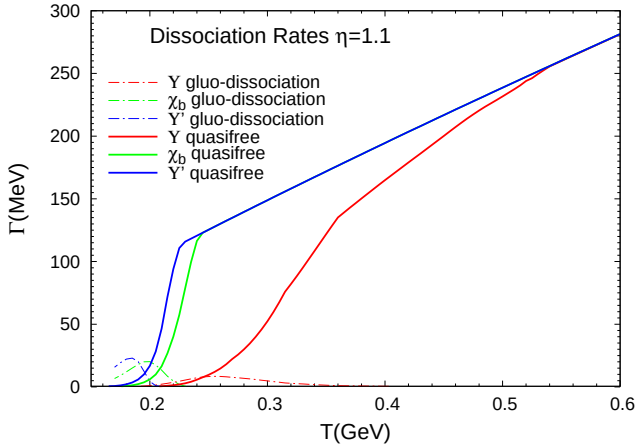

FIG. 3: Bottomonium dissociation rates for the in-medium T-matrix binding scenario (TBS) in a massive thermal parton gas. Upper panel: baseline TBS (with η=1.0 in Fig. 1); middle (lower) panel: TBS with increased (decreased) binding energies η=0.9 (η=1.1); note that η=0 recovers the SBS. The dash-dotted and solid lines correspond to gluo-dissociation and inelastic parton scattering, respectively, while red, green, and blue colors represent $\Upsilon(1S)$, $\chi_b(1P)$ and $\Upsilon(2S)$ states, respectively. Dissociation rates are evaluated at bottomonium 3-momentum p=0. Interference corrections are included in the quasifree inelastic parton scattering.

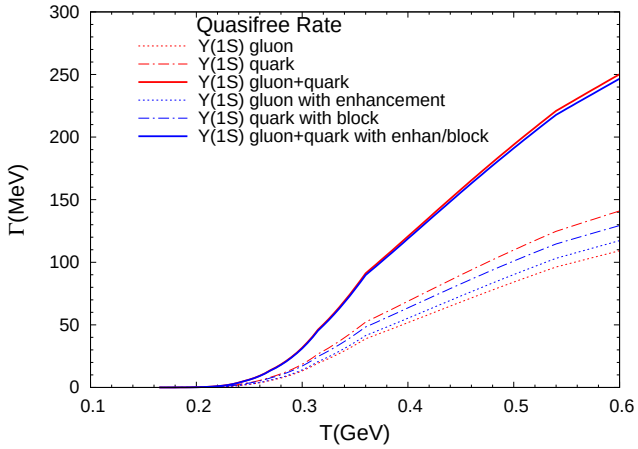

FIG. 4: Parton-induced quasifree dissociation rates (solid lines) for the baseline in-medium T-matrix binding scenario (TBS with η=1.0) in a massive thermal parton gas with (blue lines) or without (red lines) final-state Fermi blocking and Bose enhancement factors for quarks (dash-double-dotted lines) and gluons (dotted lines), respectively. The rates are evaluated at p=0 for $\Upsilon(1S)$. Interference corrections are included.

ios discussed above. Generically, gluo-dissociation differs from inelastic parton scattering in that the rate decreases with 3-momentum while that of the inelastic parton scattering increases. This is a direct consequence of the underlying matrix element (or cross section), which, as a function of incoming parton energy, peaks slightly above the binding energy for gluo-dissociation while it monotonically increases for inelastic parton scattering. The increase with p of the latter is more pronounced for larger binding energies, primarily due to the opening of phase space. For the SBS with massless partons (upper panel of Fig. 5) the p dependence for gluo-dissociation rate is rather flat at low T but starts to develop a decreasing trend for the excited states with increasing T. For the massive parton gas, this decreasing trend persists but is largely compensated once inelastic parton scattering is included (lower panel of Fig. 5).

For the TBS, the inelastic parton scattering at low T results in a marked increase of the rates with p for all Y states (upper panel of Fig. 6), mostly due to the phase space restrictions st low p imposed by the still sizable binding energies. At higher T, where the binding is much reduced, this trend weakens (lower panel of Fig. 6). Note that at T=300 MeV, both $\Upsilon(2S)$ and $\chi_b(1P)$ have essentially become unbound so that the rate corresponds to twice the b-quark scattering rate. At this temperature, the $\Upsilon(1S)$ still carries a significant binding energy which induces a more pronounced p dependence (as well as sensitivity to the binding energy). The gluo-dissociation rates in the TBS are shown in Fig. 7. Except for the $\Upsilon(1S)$ at low T (where it is still strongly bound), they exhibit the usual decreasing trend with p. They vanish for the excited states as soon as they become unbound

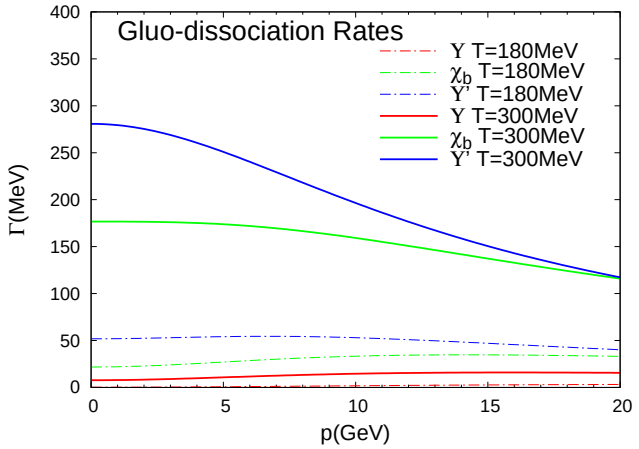

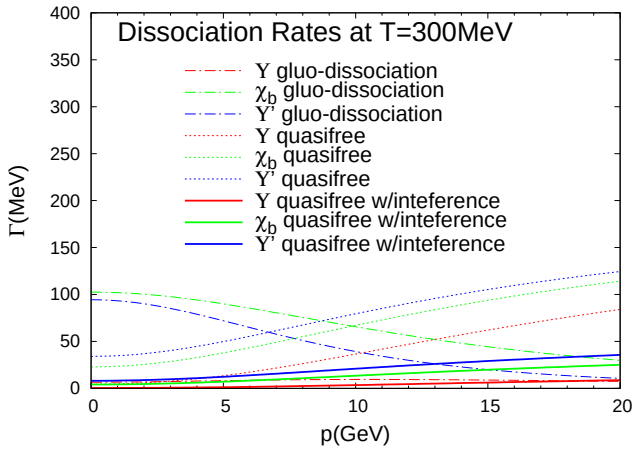

FIG. 5: Three-momentum dependence of bottomonium dissociation rates in the SBS (vacuum binding). Upper panel: gluo-dissociation with massless partons at T=180 MeV (dash-dotted lines) and T=300 MeV (solid lines). Lower panel: gluo-dissociation (dash-dotted lines) and inelastic parton scattering (solid lines) for massive partons, at a temperature of T=300 MeV. In both panels red, green and blue colors correspond to $\Upsilon(1S)$, $\chi_b(1P)$, and $\Upsilon(2S)$ states, respectively.

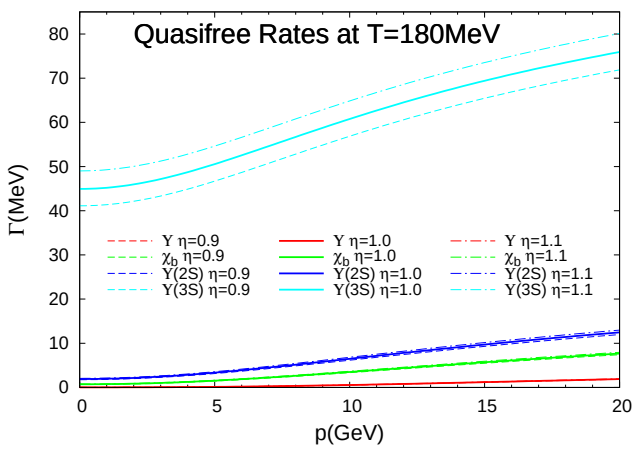

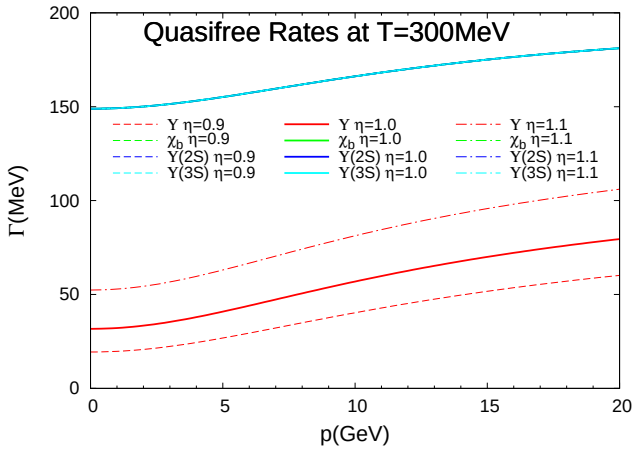

FIG. 6: Three-momentum dependence of bottomonium dissociation rates from inelastic massive-parton scattering in the TBS for T=180 MeV (upper panel) and T=300 MeV (lower panel). The solid and dash-dotted lines correspond to the baseline TBS (η=1.0) and an increased (decreased) binding with η=0.9 (η=1.1), respectively. The red, green and blue lines correspond to the Υ, $\chi_b(1P)$, and $\Upsilon(2S)$ states, respectively.

(for $T \lesssim 300$ MeV), while they are quite significant close to $T_{\rm pc}$ thus counter-balancing the increasing trend of the quasifree rate. This also applies to the $\Upsilon(1S)$ as long as its binding energy is larger than the temperature, *i.e.*, for $T \lesssim 300$ MeV.

2. *Equilibrium limit*

Detailed balance between dissociation and formation reactions implies that the long-time limit of the rate equation recovers the equilibrium abundances of quarkonia, $N_Y^{\rm eq}$ in Eq. (1). Assuming that the total number of $b\bar{b}$ pairs is conserved throughout the fireball expansion, a pertinent conservation law is formulated,

$$N_{b\bar{b}} = \frac{1}{2}\gamma_b n_{\rm op} V_{\rm FB} \frac{I_1(\gamma_b n_{\rm op} V_{\rm FB})}{I_0(\gamma_b n_{\rm op} V_{\rm FB})} + \gamma_b^2 n_{\rm hid} V_{\rm FB} \ , \qquad (7)$$

where the sum of thermal densities of open ($n_{\rm op}$) and hidden ($n_{\rm hid}$) bottom states in the system is matched to $N_{b\bar{b}}$ via a temperature-dependent fugacity factor, γ_b, for each centrality of an AA collision at given energy. The bottom densities are evaluated at each temperature according to the phase of the fireball at volume $V_{\rm FB}$, *i.e.*, with bottom quarks in the QGP for $T > T_{\rm pc}$, with bottom hadrons in the hadronic phase for $T < T_{\rm pc}$, and via a standard mixed-phase partitioning for $T = T_{\rm c}$ (if applicable, see Sec. II B for a discussion on the mixed phase). The number of $b\bar{b}$ pairs at given impact parameter is determined by the production cross section $\sigma_{pp\to b\bar{b}}$, as $N_{b\bar{b}} = (\sigma_{pp\to b\bar{b}}/\sigma_{pp}^{\rm inel}) N_{\rm coll} S_{\rm CNM}$, where $N_{\rm coll}$ denotes the number of primordial NN collisions upon first impact of the incoming nuclei and $S_{\rm CNM}$ is a shadowing correction. The thermal equilibrium value of a bottomonium state

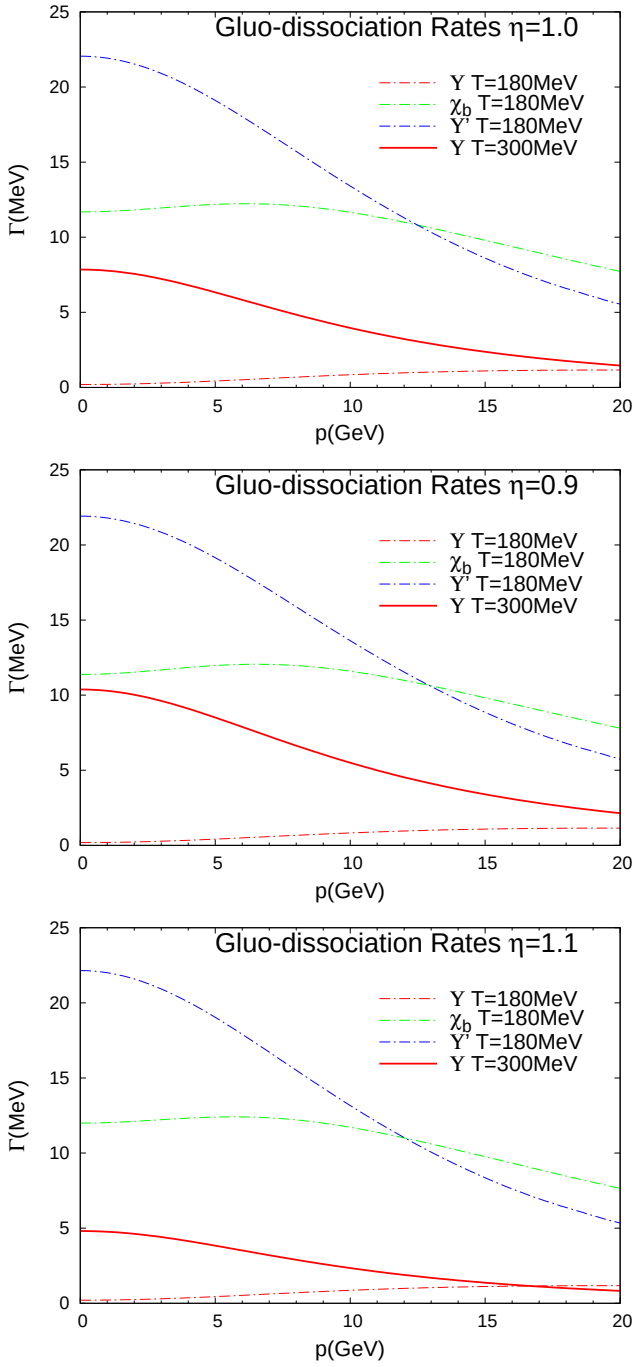

FIG. 7: Three-momentum dependence of bottomonium rates from gluo-dissociation in the TBS for the baseline scenario (η=1.0, upper panel) and increased (decreased) binding η=0.9, middle panel (η=1.1, lower panel) at T=180 MeV (dash-dotted lines) and T=300 MeV (solid lines). The red, green and blue lines correspond to the Υ, $\chi_b(1P)$, and $\Upsilon(2S)$ states, respectively.

then follows as

$$N_Y^{\rm eq}(T) = V_{\rm FB}\gamma_b^2(T) n_Y(m_Y;T) \ . \tag{8}$$

Three corrections to the equilibrium limit are in order for a more realistic implementation in URHICs, two due to chemistry and one due to kinetics (sensitivity checks of the parameters associated with these corrections will be elaborated in Sec. IV C).

The first correction concerns a finite correlation volume, $V_{\rm corr}$, which accounts for the finite distance by which a single $b\bar{b}$ can separate after essentially point-like production [42]. This limits the available phase space, which we model following our previous treatment of charmonia [11], by replacing the volume factor in the canonical suppression factor represented by the modified Bessel functions in Eq. (7) by

$$V_{\rm corr} = \frac{4}{3}\pi\left(r_0 + \langle v_b\rangle t\right)^3 \ , \tag{9}$$

that is,

$$N_{b\bar{b}} = \frac{1}{2}\gamma_b n_{\rm op} V_{\rm FB}\frac{I_1(\gamma_b n_{\rm op} V_{\rm corr})}{I_0(\gamma_b n_{\rm op} V_{\rm corr})} + \gamma_b^2 n_{\rm hid} V_{\rm FB} \ . \tag{10}$$

The initial radius of the correlation volume, $r_0\simeq$0.8-1.2 fm, characterizes a typical strong interaction range, and the recoil velocity, $\langle v_b\rangle$=0.6-0.7, is estimated from B-meson p_T spectra (we use the central values unless otherwise noted). For an increasing number of $b\bar{b}$ pairs, the individual correlation volumes may overlap, eventually merging into a single one to be used in the canonical suppression factor.

The second correction, further following our previous treatment of charmonia [13], concerns the emergence of open-bottom hadronic degrees of freedom as $T_{\rm pc}$ is approached from above (this has recently been supported in an analysis of charm susceptibilities computed in lQCD [43]). Specifically, we allow for the existence of ground-state (S-wave) open-bottom mesons B, B^*, B_s, and B_s^* with their respective spin-isospin degeneracies. The presence of such states reduces the b-quark fugacity factor and thus the equilibrium limit of the bottomonium states in the rate equation. Going up in temperature from $T_{\rm pc}$, we continuously phase out the resonance states around a switching temperature of T=220 MeV to obtain a smooth connection to b-quark only degrees of freedom, cf. Fig. 8. We will elaborate on the impact of this effect on the regeneration contribution to the Y $R_{\rm AA}$'s in nuclear collisions in Sec. IV C.

The third correction to the equilibrium limit arises from an incomplete kinetic equilibration of b quarks in URHICs, which affects the gain term in the rate equation (1). In particular, harder b-quark spectra than the thermalized limit imply a reduced phase space overlap for bound-state formation. Following Ref. [44], we model this by implementing a thermal relaxation factor into the Y equilibrium limits,

$$R(\tau) = 1 - \exp\left(-\int_{\tau_0}^{\tau}\frac{\tau'}{\tau_{\rm b}}{\rm d}\tau'\right) \ , \tag{11}$$

with a b-quark relaxation time of $\tau_{\rm b} \simeq 11\,{\rm fm}/c$ [29] at $\sim 2\,T_{\rm c}$, slowly increasing with decreasing temperature.

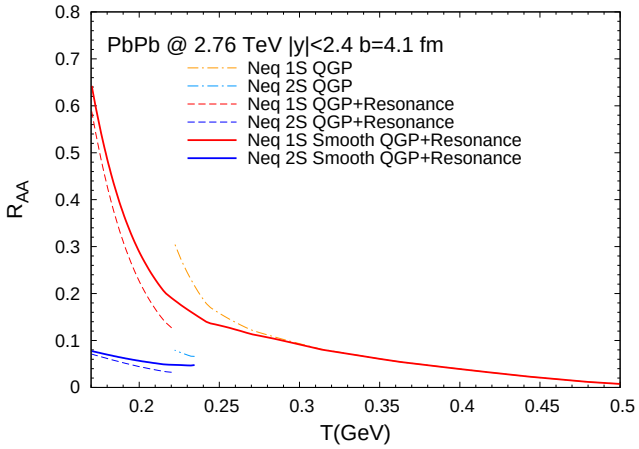

FIG. 8: Equilibrium limits of Y states with (dashed lines) and without (dash-dotted lines) B-meson resonance degrees of freedom, and their smooth interpolation (solid lines) around a switching temperature of T=220 MeV. The red (blue) and yellow (light blue) curves are for b-quark only (b-quark plus resonance) degrees of freedom for $\Upsilon(1S)$ and $\Upsilon(2S)$, respectively. The default TBS parameter η=1.0 is used.

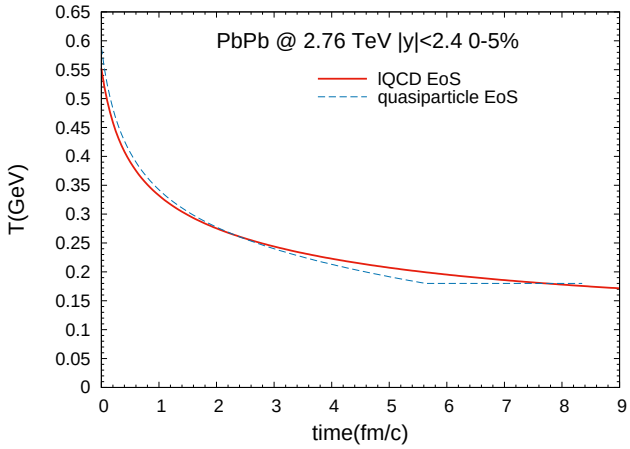

FIG. 9: Temperature evolution of the expanding firecylinder for central Pb-Pb(2.76 TeV) collisions using a lattice EoS with $T_{\rm pc}$=170 MeV (red solid line), compared to a massless quasiparticle EoS with mixed phase at $T_{\rm c}$=180 MeV (blue dashed line).

This approximation has been supported by the studies in Ref. [45].

B. Bulk medium evolution and solutions of the rate equation

To solve the rate equation, the space-time evolution of the medium is needed. We assume the conservation of total entropy in a cylindrical isotropic fireball expansion of volume

$$V_{\rm FB}(\tau) = (z_0 + v_z\tau)\pi\left(R_0 + \frac{\sqrt{a_T^2\tau^2+1}-1}{a_T}\right)^2 \quad (12)$$

with a relativistic transverse acceleration and initial transverse radius R_0 estimated from the Glauber model. The total entropy,

$$S_{\rm total} = s_{\rm QGP}(T)V_{\rm FB}(\tau)\ , \quad (13)$$

is determined from the final-state hadron multiplicities for a collision of given energy and centrality [*e.g.*, $S_{\rm tot}$=22000 for Pb-Pb(2.76TeV) covering Δy=1.8 units in rapidity]. For the QGP entropy density, $s_{\rm QGP}(T)$, we update our previous massless quasiparticle EoS with a fit to lQCD data [32] for the TBS calculation. The initial longitudinal length in the Bjorken limit is the product of the rapidity coverage of the fireball, Δy=1.8 and the QGP formation time, τ_0 [for which we use 0.2(0.6) fm at LHC (RHIC) energies], $z_0 = \Delta y\tau_0$. The relative longitudinal velocity of the two fireball fronts for Δy=1.8 corresponds to v_z=1.4, and the relativistic transverse acceleration is taken as a_T=0.1/fm. For the case of the quasiparticle EoS, we define the QGP fraction in the mixed phase as

$$f_{\rm QGP}(\tau) = \frac{s(\tau) - s_{\rm HG}(T_c)}{s_{\rm QGP}(T_c) - s_{\rm HG}(T_c)} \quad (14)$$

where $s(\tau) = S_{\rm total}/V_{\rm FB}(\tau)$, $s_{\rm HG}(T_c)$ is the entropy density of the hadron gas at $T_{\rm c}$=180 MeV (as used previously), and $f_{\rm HG}(\tau) = 1 - f_{\rm QGP}(\tau)$. The resulting time evolutions of temperature for central Pb-Pb(2.76 TeV) collisions for the massless quasiparticle EoS and the updated lQCD EoS are compared in Fig. 9. The nonperturbative effects lead to slightly higher (lower) temperatures in the transition (high-temperature) region, as well as the absence of a mixed phase. The lifetimes at the end of the QGP/mixed phase are within ∼10%.

We now have all ingredients to solve the rate equation. For later purposes, we will decompose it into two parts. The suppression-only (or primordial) part is obtained from

$$\frac{{\rm d}N_Y^{\rm prim}(\tau)}{{\rm d}\tau} = -\Gamma_Y(\tau)N_Y^{\rm prim}(\tau)\ , \quad (15)$$

which has the solution

$$N_Y^{\rm prim}(\tau) = N_Y^{\rm prim}(\tau_0)\,\exp\left(-\int_{\tau_0}^{\tau}\Gamma_Y(\tau'){\rm d}\tau'\right)\ , \quad (16)$$

characterizing the primordially produced bottomonia which survive the fireball evolution. On the other hand, subtracting the rate equation of the primordial component from the total one yields an equation for the regenerated component,

$$\frac{{\rm d}N_Y^{\rm reg}(\tau)}{{\rm d}\tau} = -\Gamma_Y(\tau)\left[N_Y^{\rm reg}(\tau) - N_Y^{\rm eq}(\tau)\right], \quad (17)$$

whose solution can also be written in a closed form as

$$N_Y^{\rm reg}(\tau) = \frac{\int\limits_{\tau_{\rm diss}}^{\tau} \Gamma_Y(\tau') N_Y^{\rm eq}(\tau') \exp\left(\int\limits_{\tau_{\rm diss}}^{\tau'} \Gamma_Y(\tau'')\mathrm{d}\tau''\right)\mathrm{d}\tau'}{\exp\left(\int\limits_{\tau_{\rm diss}}^{\tau} \Gamma_Y(\tau'')\mathrm{d}\tau''\right)} = \int\limits_{\tau_{\rm diss}}^{\tau} \Gamma_Y(\tau') N_Y^{\rm eq}(\tau') \mathrm{e}^{-\int\limits_{\tau'}^{\tau}\Gamma_Y(\tau'')\mathrm{d}\tau''}\mathrm{d}\tau' \qquad (18)$$

where the total lifetime of the fireball, τ=$\tau_{\rm f}$, is given by the end of the QGP/mixed phase. The exponential factor $\mathrm{e}^{-\int_{\tau'}^{\tau}\Gamma_Y(\tau'')\mathrm{d}\tau''}$ in the last line represents the in-medium suppression of the regenerated quarkonia. The lower integration bound $\tau_{\rm diss}$ characterizes the time in the fireball evolution where the temperature has dropped to the dissociation temperature of a given Y state, below which regeneration becomes operative. For the TBS, we have $T_{\rm diss}$≃260 MeV, 240 MeV and 190 MeV for $\chi_b(1P)$, $\Upsilon(2S)$ and $\Upsilon(3S)$, respectively. The initial condition, $N_Y^{\rm prim}(\tau_0) = N_{\rm coll}\frac{\sigma_{pp\to Y}^{\rm tot}}{\sigma_{pp}^{\rm inel}} S_{\rm CNM}^Y$ for the Y numbers includes CNM effects, in particular nuclear shadowing, calculated from the Glauber model (nuclear absorption is included at the RHIC but neglected at the LHC due to the short nuclear passage time).

C. Transverse-momentum spectra and elliptic flow

The rate equation approach above provides the 3-momentum inclusive yields of the produced bottomonia. The explicit 3-momentum dependence of the yields can be recovered in an approximate way by utilizing the decomposition into primordial and regenerated components discussed above, following Ref. [46]. For the primordial component, one straightforwardly solves the space-time dependent Boltzmann equation for the bottomonium phase space distribution function while for the regeneration component a coalescence model is employed. This is elaborated in more detail in the respective Secs. II C 1 and II C 2, while Sec. II C 3 discusses our evaluation of the bottomonium elliptic flow.

1. *Transverse-momentum spectra of surviving primordial bottomonia*

Without a gain term (and without a mean field), the Boltzmann transport equation for the bottomonium phase space distribution, f_Y, reads

$$\frac{\partial f_Y(\vec{x},\vec{p},\tau)}{\partial\tau} + \vec{v}\cdot\frac{\partial f_Y(\vec{x},\vec{p},\tau)}{\partial\vec{x}} = -\Gamma_Y(\vec{p},T(\tau)) f_Y(\vec{x},\vec{p},\tau) \qquad (19)$$

where $\vec{v}=\vec{p}/E_p$ denotes the bottomonium velocity ($E_p^2 = m_Y^2+p^2$) and $\Gamma_Y(p,T)$ the 3-momentum dependent dissociation rate (as displayed in Figs. 5, 6, and 7). Its solution can be cast in the form

$$f_Y(\vec{x},\vec{p},\tau) = f_Y(\vec{x}-\vec{v}(\tau-\tau_0),\vec{p},\tau_0)\mathrm{e}^{-\int\limits_{\tau_0}^{\tau}\Gamma_Y(\vec{p},T(\tau'))\mathrm{d}\tau'}, \qquad (20)$$

from which p_T spectra can be extracted assuming boost invariance as

$$\frac{\mathrm{d}^2N_Y(p_T,\phi)}{\mathrm{d}^2p_T} = \int f_Y(\vec{x}_T,\vec{p}_T,\tau) d^2x_T\ . \qquad (21)$$

The initial phase-space distribution, $f_Y(\vec{x},\vec{p}_T,\tau_0) = f_Y^{\rm Glb}(\vec{x}) f_Y^{\rm AA}(\vec{p}_T)$, is factorized into p_T spectra taken from experimental data in pp collisions and a Glauber model for the spatial distribution,

$$f_Y^{\rm Glb}(\vec{x}_T) = \int \rho_A(\vec{x}_T+\vec{b}/2,z)\rho_A(\vec{x}_T-\vec{b}/2,z')\mathrm{d}z\mathrm{d}z' \qquad (22)$$

for an AA collision at impact parameter b.

We furthermore include formation time effects [47–49] to account for the finite time for the bound state to develop from the primordially produced $b\bar{b}$ wave package. This evolution tends to reduce the suppression rate, intuitively associated with a geometric expansion of the wave package from its near point-like production to the bound-state size [50]. Accordingly, we assume the formation time $\tau_{\rm form}$ to depend on the vacuum binding energy, and correct the dissociation rate for $\tau \le \tau_{\rm form}\gamma$ as

$$\alpha_Y(\vec{p},T(\tau)) \equiv \Gamma_Y(\vec{p},T(\tau))\frac{\tau}{\tau_{\rm form}}\frac{m_Y}{\sqrt{p^2+m_Y^2}}\ . \qquad (23)$$

in the (early) evolution of the primordial p_T spectra. The explicit formation time values for $\Upsilon(1S)$, $\Upsilon(2S)$ and $\Upsilon(3S)$ are chosen as 0.5, 1.0 and 1.5 fm, respectively. The latter two are close to typical values used for the J/ψ and χ_c, as they have comparable binding energies [$E_B(J/\psi)$≃640 MeV vs. $E_B(\Upsilon(2S))$≃540 MeV, and $E_B(\chi_c)$≃230 MeV vs. $E_B(\Upsilon(3S))$≃200 MeV]. The inverse Lorentz-γ factor, $\gamma^{-1} = \frac{m_Y}{\sqrt{p^2+m_Y^2}}$, suppresses the high-$p_T$ reaction rates especially for excited states which have larger formation times. The reduced primordial suppression at high p_T counterbalances the p_T dependence in the thermal dissociation rates.

2. *Transverse-momentum spectra from regeneration*

The momentum spectra of regenerated quarkonia carry the imprint of the momentum distributions of the recombining heavy quarks (or mesons). For charmonia, the regeneration typically occurs several fm/c into the evolution of the fireball, where charm-quark spectra, with a

thermal relaxation rate of a few fm/c, are probably not far from their equilibrium distribution. Thus, the regenerated charmonia can be rather well approximated by a blast-wave description close to $T_{\rm pc}$, which is supported by the momentum spectra measured at the LHC [10]. The situation changes for bottom(onium), primarily because the $\sim$3 times larger b-quark mass, relative to c quarks, implies a factor 3 longer thermal relaxation times, and, to a lesser extent, because bottomonia are formed earlier in the fireball evolution, due to their larger binding energies. Therefore, approximating regenerated bottomonia with a thermal blast-wave expression cannot be expected to be accurate. Instead, we here resort to an instantaneous coalescence model [51], which allows us to use more realistic nonequilibrium transverse-momentum spectra of b quarks as input. We take these spectra from relativistic Langevin simulations of heavy quarks [33] in a hydrodynamic background medium (akin to the fireball evolution used for the rate equation) with nonperturbative heavy-quark transport coefficients which are computed from the same underlying T-matrix interactions [29] as the bottomonium binding energies discussed in Sec. II A 1.

The expression for the 2-differential p_T spectra of an Y meson formed through instantaneous coalescence from bottom quark and antiquarks with p_t distributions, $\mathrm{d}^2N_{b,\bar{b}}/\mathrm{d}^2p_T$ (or $\mathrm{d}^2N_Y^{\rm coal}/\mathrm{d}^2p_T$), is given by [51]

$$\begin{aligned}\frac{\mathrm{d}^2N_Y^{\rm coal}(p_T,\phi)}{\mathrm{d}^2p_T} &= C_{\rm reg}\int \mathrm{d}^2p_{1t}\mathrm{d}^2p_{2t}\frac{\mathrm{d}^2N_b}{\mathrm{d}^2p_{1t}}\frac{\mathrm{d}^2N_{\bar{b}}}{\mathrm{d}^2p_{2t}}\\ &\times\delta^{(2)}(\vec{p}_T-\vec{p}_{1t}-\vec{p}_{2t})\\ &\times\Theta\left[\Delta_p^2-\frac{(\vec{p}_{1t}-\vec{p}_{2t})^2}{4}+\frac{(m_{1t}-m_{2t})^2}{4}\right].\end{aligned} \tag{24}$$

Here, $C_{\rm reg}$ denotes a normalization constant which is matched to the regeneration yield obtained from the rate equation, and $m_t=\sqrt{p_t^2+m_b^2}$ is the transverse mass of the b quarks. The Θ function characterizes the momentum space wave function of the formed Y, suppressing high relative momenta of the coalescing b quarks. The covariant momentum space radius, Δ_p, is inversely proportional to the coordinate-space radius via the uncertainty relation, $\Delta_p\Delta_x\simeq 1$. We use $\Delta_x\simeq r_{\Upsilon[\Upsilon(2S),\chi_b(1P)]}=0.2[0.5]\,\mathrm{fm}$. The p_T spectra are obtained by integrating the 2-differential spectrum in Eq. (24) over the azimuthal angle,

$$\frac{\mathrm{d}N_Y^{\rm coal}(p_T)}{\mathrm{d}p_T}=\int_0^{2\pi}\frac{\mathrm{d}^2N_Y^{\rm coal}(p_T,\phi)}{\mathrm{d}^2p_T}p_T\mathrm{d}\phi\ . \tag{25}$$

As an estimate of the uncertainty in the regeneration time, we will adopt snapshots of the evolving b-quark distributions from the Langevin simulations at different local temperatures with pertinent flow velocities in the underlying hydro evolution of Ref. [33].

Finally, to account for the p_T dependence of the formation rate, which is not captured by the instantaneous coalescence approximation, we weight the coalescence spectrum, Eq. (25), by the p_T dependence of the inelastic reaction rate,

$$\frac{dN_Y^{\rm reg}}{dp_T}=\hat{\Gamma}_Y(p_T,\bar{T}_{\rm reg})\frac{\mathrm{d}N_Y^{\rm coal}}{\mathrm{d}p_T} \tag{26}$$

where $\hat{\Gamma}_Y(p_T,\bar{T}_{\rm reg})\equiv\Gamma_Y(p_T,\bar{T}_{\rm reg})/\bar{\Gamma}_Y(\bar{T}_{\rm reg})$ includes a normalization $\bar{\Gamma}_Y$ such that the norm of the regeneration component as obtained from the rate equation is preserved.

3. *Elliptic flow*

Another observable with a potential to disentangle primordially produced and regenerated quarkonia is their elliptic flow. It is quantified by the second coefficient, $v_2(p_T)$, in the the Fourier expansion of their azimuthal-angle differential distribution,

$$\frac{\mathrm{d}^2N}{\mathrm{d}^2p_T}=\frac{1}{2\pi}\frac{\mathrm{d}N(p_T)}{p_T\mathrm{d}p_T}[1+2v_2(p_T)\cos(2\phi)+\dots], \tag{27}$$

where ϕ is defined relative to the x axis, which lies in the reaction plane aligned with the impact parameter. At mid-rapidity, odd harmonics are suppressed, while higher even harmonics ($v_4,v_6,\dots$) for bulk hadron production are typically much smaller than v_2. From the above expansion one projects out the second coefficient via

$$v_2(p_T)=\frac{\frac{1}{2\pi}\int_0^{2\pi}\frac{\mathrm{d}^2N(p_T,\phi)}{p_T\mathrm{d}p_T\mathrm{d}\phi}\cos(2\phi)\mathrm{d}\phi}{\frac{1}{2\pi}\int_0^{2\pi}\frac{\mathrm{d}^2N(p_T,\phi)}{p_T\mathrm{d}p_T\mathrm{d}\phi}\mathrm{d}\phi}\ . \tag{28}$$

For the primordial component, we explicitly track the bottomonium paths through an elliptically expanding fireball; the pertinent $v_2^{\rm prim}$ is generated entirely due to path length differences and usually rather small in magnitude [52] (contributions from elastic scatterings are not accounted for; little is known about such processes). For the regeneration component, the coalescence expression, Eq. (24), incorporates the v_2 information through the convolution of the underlying b- and $\bar{b}$-quark flows. The total elliptic flow follows as the weighted sum of the two contributions,

$$v_2(p_T)=\frac{R_{AA}^{\rm prim}(p_T)v_2^{\rm prim}(p_T)+R_{AA}^{\rm coal}(p_T)v_2^{\rm coal}(p_T)}{R_{AA}^{\rm prim}(p_T)+R_{AA}^{\rm coal}(p_T)}\ . \tag{29}$$

D. Open-bottom and bottomonium input cross sections

The basic quantity to compute below is the nuclear modification factor, defined as the ratio of yields in an

p_T[GeV]	$\chi_b(1P)$[%]	$\chi_b(2P)$[%]	$\chi_b(3P)$[%]	total $\chi_b(nP)$[%]
6∼8	14.8	3.3		18.1
8∼10	17.2	5.2		22.4
10∼14	21.3	4.0	1.7	27.0
14∼18	24.4	5.2	1.8	31.4
18∼22	27.2	5.5	1.9	34.6
22∼40	29.2	6.0	2.9	38.1

TABLE I: Feeddown fractions from $\chi_b(nP)$ states to $\Upsilon(1S)$ from LHCb [53].

AA collision at a given centrality divided by the $N_{\rm coll}$-scaled yield in pp,

$$R_{\rm AA} = \frac{N_Y^{\rm AA}}{N_{\rm coll}\frac{\sigma_{pp\to Y}}{\sigma_{pp}^{\rm inel}}} \ . \tag{30}$$

This has been measured as a function of several variables, *i.e.*, nucleon participant number ($N_{\rm part}$) as a measure of centrality (which we estimate from the optical Glauber model), transverse momentum (p_T), rapidity (y), and collision energy ($\sqrt{s}$). The numerator in Eq. (30) contains the primordial component, which is also proportional to the product of $N_{\rm coll}\sigma_{pp\to Y}$ (times a suppression factor), and the regeneration component, which is largely controlled by the open-bottom cross section, $\sigma_{pp\to b\bar{b}}$, independent of the denominator (although in practice we will assume a proportionality between open- and hidden-bottom cross sections).

Feeddowns from higher excited states contribute to the inclusive production of an observed meson. A detailed summary of feeddown fractions can be found in Appendix B. For the p_T-dependent $R_{\rm AA}$'s at both RHIC and LHC energies, we include the p_T dependence of the feeddown in our calculations. By using harder p_T spectra for excited states, but with the same branching fraction as at low p_T, we automatically obtain a larger feeddown at high p_T which is essentially consistent with LHCb Collaboration data [53]; cf. Table I.

We slightly update several input cross sections for the TBS calculations relative to Ref. [28], as summarized in Table II, but keep the ratio $\frac{\sigma_Y}{\sigma_{b\bar{b}}} \simeq 0.176\,\%$ as in our previous work which is within the uncertainty of measured values. This ratio only affects the regeneration component of $R_{\rm AA}$. In general, the small pp cross sections for $b\bar{b}$ pairs render their number less than 1 even in AA collisions at the LHC. Therefore, the corresponding Y equilibrium limits are in the canonical limit, so that $R_{\rm AA}^{\rm reg}$ is essentially linear in $\frac{\sigma_Y}{\sigma_{b\bar{b}}}$, and thus approximately constant for not too peripheral collisions (for the latter, the small QGP lifetime implies that the relaxation time approximation for b-quark diffusion will lead to a noticeable suppression). Overall, our results for the $R_{\rm AA}$'s will be influenced insignificantly by the update of the input pp cross sections.

For the bottomonium input cross sections at $\sqrt{s}$=200 GeV we adopt the STAR measurement [54] of $\Upsilon(1S+2S+3S)$, $\frac{{\rm d}\sigma}{{\rm d}y}\cdot Br(\mu\bar{\mu}) = 81 \pm 5 \pm 8\,pb$. We reconstruct σ_{1S}^{tot} using the di-muon branching ratios $Br(1S\to\mu\bar{\mu}) = 2.48\,\%$, $Br(2S\to\mu\bar{\mu}) = 1.93\,\%$, and $Br(3S\to\mu\bar{\mu}) = 2.18\,\%$ with cross sections $\sigma_{2S} = 0.33\sigma_{1S}^{tot}$ and $\sigma_{3S} = 0.15\sigma_{1S}^{tot}$ (see Appendix B), so that $\frac{{\rm d}\sigma_{1S}^{tot}}{{\rm d}y} = \frac{81\,pb}{1\cdot 2.48\,\%+0.33\cdot 1.93\,\%+0.15\cdot 2.18\,\%} \simeq 2.35\,nb$. We use the same values for open-bottom cross section as in previous work [28], *i.e.*, $\sigma_{pp\to b\bar{b}}$=3.2 μb, with a factor of 0.52 to obtain $\sigma_{pp\to b\bar{b}}$=1.67μb in one fireball (Δy=1.8), or $\frac{{\rm d}\sigma_{pp\to b\bar{b}}}{{\rm d}y}$=0.92 μb. This is consistent with the most recent PHENIX results [55]. For simplicity, we use the same input values for uranium-uranium (U-U) collisions at 193 GeV.

For pp collisions at 2.76 TeV, we use the the inclusive $\Upsilon(1S)$ cross section of $\frac{{\rm d}\sigma_{pp\to\Upsilon(1S)}}{{\rm d}y}$=30.3 nb for $|y|$<2.4 based on CMS pp data [31], which is ∼25% smaller than in Ref. [28]. With $\frac{\sigma_{\Upsilon(1S)}}{\sigma_{b\bar{b}}} \simeq 0.176\,\%$ this gives $\frac{{\rm d}\sigma_{pp\to b\bar{b}}}{{\rm d}y}$=17.2 μb at 2.76 TeV for $|y|$<2.4 which is consistent with the upper range of FONLL calculations [56], 15±6.2 μb. We estimate a 10 % reduction from $|y|$<0.9 to $|y|$<2.4. From a comparison of 7 TeV ALICE [57] and CMS [58] data, we estimate the forward-rapidity (2.5<$|y|$<4.0) cross section at about 45 % of the mid-rapidity ($|y|$<0.9) value, or 50 % of the ($|y|$<2.4) value. The $\Upsilon(2S)$ cross section is about 33 % of inclusive $\Upsilon(1S)$ as discussed in Appendix B.

At 5.02 TeV, we adopt for the inclusive $\Upsilon(1S)$ cross section the recent CMS pp reference [59, 60], $\frac{{\rm d}\sigma_{pp\to Y}}{{\rm d}y}$=64.0 nb (57.6 nb) for $|y| < 0.9$ ($|y| < 2.4$), together with the $\Upsilon(1S)$ over open-bottom ratio of 0.176 % and the same reduction of 55 % (50 %) from mid-rapidity $|y| < 0.9$ ($|y| < 2.4$) to forward rapidity $2.5 < y < 4.0$.

The absolute input cross sections at different energies for different states for the TBS calculations are summarized in Table. II.

III. BOTTOMONIUM PRODUCTION AT RHIC

We are now in position to present our numerical results for bottomonium observables in comparison to experimental data, starting with RHIC energies. Before presenting and discussing the results for the centrality and p_T dependencies in Secs. III A and III B, let us briefly outline our implementation of CNM effects, which we estimate from d-Au collisions. We assume no shadowing on open-bottom and bottomonium production and interpret the STAR measurement of $R_{\rm dAu}(1S) = 0.83 \pm 0.15({\rm dAu_{stat}}) \pm 0.1(pp_{\rm stat}) \pm 0.03$ (sys) [20] as being due to nuclear absorption with a YN absorption cross section in a range of $\sigma_Y^{\rm abs}$=0-3 mb (identical for all bottomonia).

Differential cross section $\frac{d\sigma}{dy}$	0.20 TeV	2.76 TeV	5.02 TeV
pp$\to \Upsilon(1S)(|y|<0.5)$[nb]	2.35	-	-
pp$\to \Upsilon(1S)(|y|<2.4)$[nb]	-	30.3	57.6
pp$\to \Upsilon(1S)(2.5<y<4.0)$[nb]	-	15.1	28.8
pp$\to \Upsilon(2S)(|y|<0.5)$[nb]	0.77	-	-
pp$\to \Upsilon(2S)(|y|<2.4)$[nb]	-	10.0	19.0
pp$\to \Upsilon(2S)(2.5<y<4.0)$[nb]	-	5.0	9.5
pp$\to b\bar{b}(|y|<0.5)[\mu$b]	0.92	-	-
pp$\to b\bar{b}(|y|<2.4)[\mu$b]	-	17.2	32.7
pp$\to b\bar{b}(2.5<y<4.0)[\mu$b]	-	8.6	16.4

TABLE II: Summary of input cross sections extracted from pp collisions used in our calculations. The $\frac{d\sigma_{pp\to\Upsilon}}{dy}$ values at 200 GeV are based on STAR data [54]. The value for $\frac{d\sigma_{pp\to b\bar{b}}}{dy}$ is adopted from previous work [28] which is consistent with PHENIX results [55]. The $\frac{d\sigma_{pp\to\Upsilon}}{dy}$ values at 2.76 and 5.02 TeV for $|y|<2.4$ are based on CMS data [31, 59, 60], with a fixed $\frac{\sigma_{pp\to\Upsilon}}{\sigma_{pp\to b\bar{b}}}$ ratio of 0.176 %, as in previous work [28]. A 50 % reduction in the cross sections is assumed when going from mid-rapidity ($|y|<2.4$) to forward rapidity ($2.5<y<4.0$) [57, 58].

A. Centrality Dependence at RHIC

Our results for the $R_{\rm AA}(N_{\rm part})$ for inclusive $\Upsilon(1S)$ and $\Upsilon(1S+2S+3S)$ states in Au-Au and U-U collisions are shown in Figs. 10 and 11, respectively, in comparison to RHIC data. We focus on the T-matrix binding scenario (TBS) with baseline binding strength, η=1.0. The suppression of the inclusive $\Upsilon(1S)$ yield (upper panels) is mostly due to the excited states (as well as nuclear absorption), which manifests itself as a stronger suppression in the combined $R_{\rm AA}$ of $\Upsilon(1S+2S+3S)$ [middle (lower) panel in Fig. 10 (11)]. Primordial production dominates but regeneration, in the canonical limit with $N_{b\bar{b}}<1$ even in central collisions, is non-zero. Our results for U-U show slightly more suppression than for Au-Au, and both are generally consistent with the data.

B. Transverse-momentum dependence at RHIC

We proceed to compute Y p_T spectra by utilizing their $R_{\rm AA}$'s for primordial and regenerated components as obtained in the previous section to form the weighted sum

$$R_{\rm AA}(p_T) = \frac{\frac{dN_Y^{\rm prim}}{p_T dp_T}+\frac{dN_Y^{\rm reg}}{p_T dp_T}}{N_{\rm coll}\frac{dN_Y^{pp}}{p_T dp_T}} = R_{\rm AA}^{\rm prim}\frac{\frac{d\hat{N}_Y^{\rm prim}}{p_T dp_T}}{\frac{d\hat{N}_Y^{pp}}{p_T dp_T}}+R_{\rm AA}^{\rm reg}\frac{\frac{d\hat{N}_Y^{\rm reg}}{p_T dp_T}}{\frac{d\hat{N}_Y^{pp}}{p_T dp_T}} \quad (31)$$

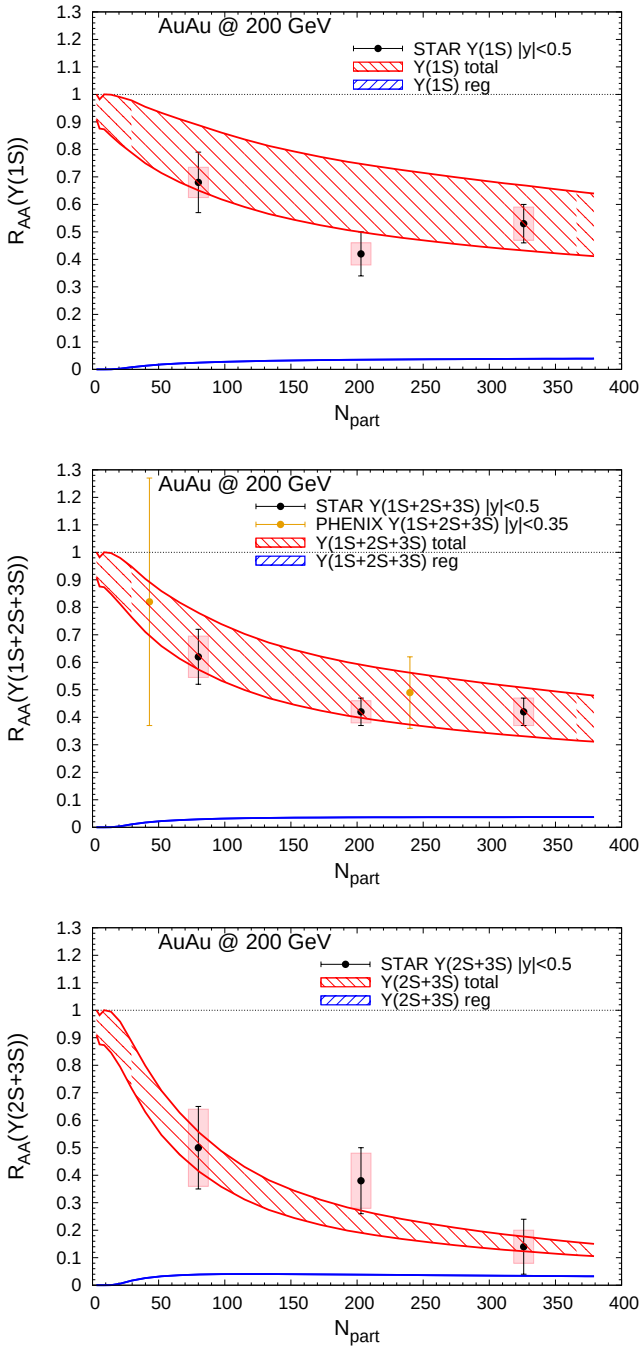

FIG. 10: Centrality dependence of bottomonium yields in Au-Au(200 GeV) collisions using the baseline TBS ($\eta=1.0$) with updated feeddowns. The total (red band) and regenerated (blue lines) contributions are shown for inclusive $\Upsilon(1S)$ (upper panel), $\Upsilon(1S+2S+3S)$ (middle panel), and $\Upsilon(2S+3S)$ (lower panel) production at mid-rapidity ($|y|$<0.5) and compared to STAR [54] and PHENIX [21] data. The band width of the total yields is due to CNM effects with $\sigma_Y^{\rm abs}$=0-3 mb [20].

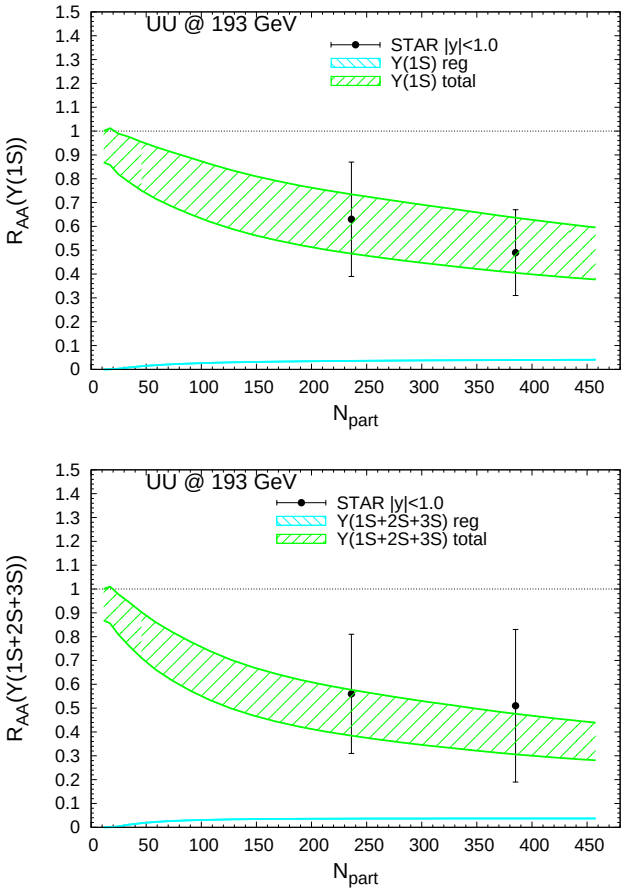

FIG. 11: Centrality dependence of bottomonium yields in U-U(193 GeV) collisions using the baseline TBS with updated feeddowns. The total (green band) and regenerated (light-blue line) contributions are shown for inclusive $\Upsilon(1S)$ (upper panel) and $\Upsilon(1S+2S+3S)$ (lower panel) at mid-rapidity ($|y|$<1.0) and compared to STAR data [22]. The band width of the total yields is due to CNM effects with $\sigma_Y^{\rm abs}$=0-3 mb [20].

where the "hat" indicates a normalized distribution,

$$\int_0^\infty p_T \mathrm{d}p_T \frac{\mathrm{d}\hat{N}(p_T)}{p_T \mathrm{d}p_T} = 1 \ , \tag{32}$$

and the $R_{\rm AA}$ coefficients represent a given centrality class, *e.g.*, 0-60 %. For the normalized pp spectra, we employ an empirical parametrization,

$$\frac{\mathrm{d}^2\hat{N}_{pp}(p_T)}{\mathrm{d}^2 p_T} = \frac{N}{\left(1+\left(\frac{p_T}{D}\right)^2\right)^A} \tag{33}$$

with fit parameters A=3.0 and D=5.3 GeV estimated from m_T scaling from charmonium p_T spectra [13] as baseline. The p_T-dependent $R_{\rm AA}$ for 0-60% Au-Au(200 GeV) is shown in Fig. 12. It tends to slightly overestimate the STAR data, although the lower end of the band (with maximal nuclear absorption) is close to the data, a trend which is also reflected in the centrality-dependent $R_{\rm AA}$ (recall the upper panel of Fig. 10)

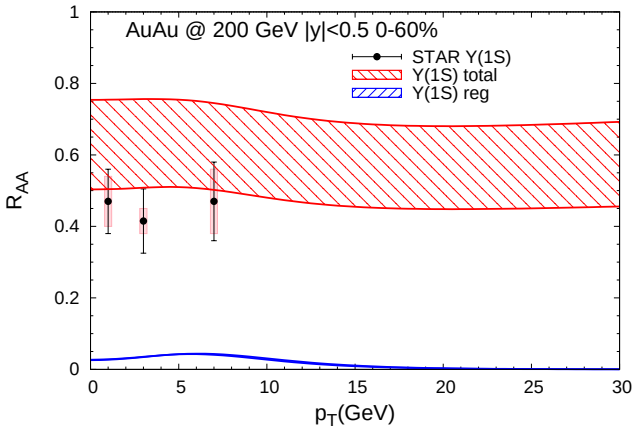

FIG. 12: The p_T-dependent $R_{\rm AA}$ for inclusive $\Upsilon(1S)$ in 0-60 % Au-Au(200 GeV) collisions within the baseline TBS, compared to STAR data [54]. The red (blue) band is for the total (regeneration) yield, where the band width of the former is due to CNM effects with $\sigma_Y^{\rm abs}$=0-3 mb [20].

IV. BOTTOMONIUM PRODUCTION IN 2.76 TEV PB-PB COLLISIONS

Turning to Pb-Pb collisions at the LHC, we first focus on $\sqrt{s}$=2.76 TeV. To make contact with the earlier employed SBS [28], we start by revisiting the inclusive $R_{\rm AA}$'s for $\Upsilon(1S)$ and $\Upsilon(2S)$ within the SBS approach (with vacuum binding energies, massless gluo-dissociation rates and a quasiparticle EoS, and input cross sections as used in Ref. [28] with an up to 25% shadowing in central collisions for both open bottom and bottomonia), but with updated feeddown fractions [albeit neglecting explicit feeddown from $\Upsilon(3S)$ and $\chi_b(2P)$ states]. We then turn to the TBS calculation with all updates included, also treating $\Upsilon(3S)$ and $\chi_b(2P)$ and their feeddown contributions explicitly.

A. Centrality dependence for SBS

We compare the feeddown-updated SBS to the recent CMS data [31] in Fig. 13; we find fair agreement with the strong $\Upsilon(2S)$ suppression while the $\Upsilon(1S)$ yields tend to be somewhat overestimated, essentially due to the now smaller feeddown. The stronger suppression exhibited by the forward-rapidity ALICE data [26] cannot be reproduced, as before. The $b\bar{b}$ production cross sections do not vary strongly enough with rapidity to generate the extra suppression. In particular, the regeneration contribution at this energy does not provide a quadratic dependence on the open-bottom cross section since the bottom yields

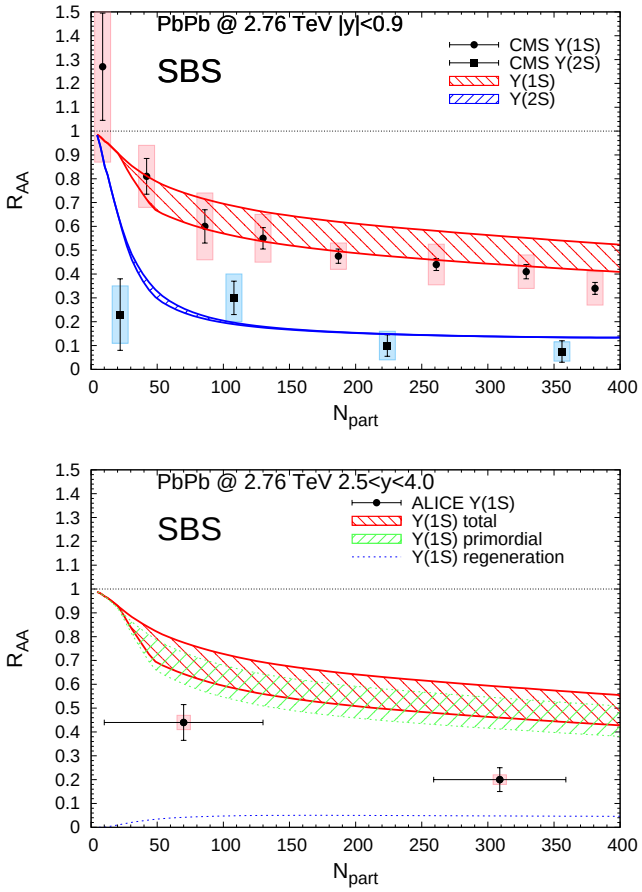

FIG. 13: Centrality dependence of bottomonium production in Pb-Pb(2.76 TeV) collisions within the SBS [28] with updated feeddowns. Upper panel: $\Upsilon(1S)$ (red band) and $\Upsilon(2S)$ (blue band) at mid-rapidity compared to CMS data [31]. Lower panel: $\Upsilon(1S)$ at forward rapidity compared to ALICE data [26], where we also show the regeneration contribution (dotted line). The band widths of the totals in both panels are due to a 0-25% variation in the shadowing suppression of the initial bottomonium yields.

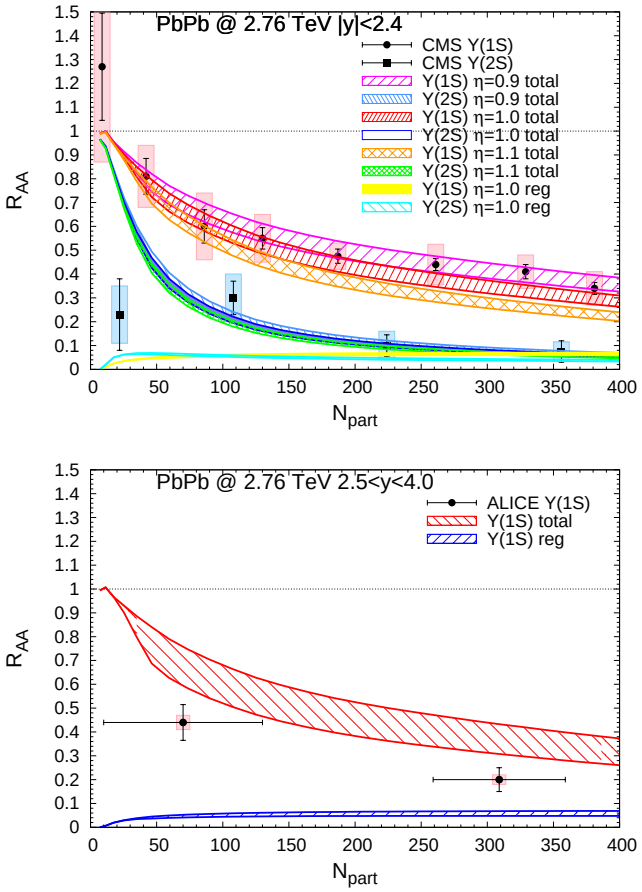

FIG. 14: Centrality dependence of $\Upsilon(1S)$ and $\Upsilon(2S)$ production in Pb-Pb(2.76 TeV) collisions within the TBS. Upper panel: inclusive $\Upsilon(1S)$ and $\Upsilon(2S)$ results at mid-rapidity for η=0.9, η=1.0 and η=1.1 scenarios compared to CMS data [31]. The red (blue) band is the total $\Upsilon(1S)$ ($\Upsilon(2S)$) $R_{\rm AA}$ for baseline η =1.0, the pink (light blue) band is the total $\Upsilon(1S)$ ($\Upsilon(2S)$) $R_{\rm AA}$ for η=0.9, the orange (green) band is the total $\Upsilon(1S)$ ($\Upsilon(2S)$) $R_{\rm AA}$ for η=1.1, and the yellow (cyan) band is the $\Upsilon(1S)$ ($\Upsilon(2S)$) regeneration contribution with η=1.0. The regeneration components for different scenarios have tiny differences. The bands reflect the uncertainty due to shadowing between 0-15%. Lower panel: inclusive $\Upsilon(1S)$ (red band) and regenerated component (blue band) at forward rapidity for η=1.0, compared to ALICE data [26]; the bands reflect the uncertainty due to a shadowing reduction between 0-30%.

are in the canonical limit, *i.e.*, with no more than one $b\bar{b}$ pair in the fireball.

B. Centrality Dependence for TBS

Next we turn to the results of our updated approach based on the TBS. Aside from the cross section inputs, CNM effects are implemented via a shadowing suppression of both open bottom and bottomonia of up to 15 % at mid-rapidity, estimated from EPS09 NLO calculations [61] and ATLAS p-Pb data for $\Upsilon(1S)$ [62], and up to 30 % at forward/backward rapidity from p-Pb data from LHCb [63] and ALICE [64].

The baseline TBS (with η=1.0) provides a fair description of the recent CMS data [31] for both $\Upsilon(1S)$ and $\Upsilon(2S)$ data; cf. upper panel of Fig. 14. Compared to the (feeddown-updated) SBS shown in the previous figure, the additional $\Upsilon(1S)$ suppression appears to be less than one might have expected given the much reduced binding energies. The main reason for this is the now massive thermal quasiparticles in the dissociation rates (as dictated by a more realistic EoS), which render gluodissociation ineffectively. The addition of the quasifree rates within the TBS leads to an overall increase of the rates compared to the SBS, but not by much. The inclusion of correlation volume effects leads to an increase of the regeneration component, while the B-meson reso-

nance states close to $T_{\rm pc}$ reduce it. Regeneration is relatively small for the ground state, but amounts to about $\sim$50% of the $\Upsilon(2S)$ yield in central collisions. This is somewhat smaller than in the SBS where it is the dominant contribution, which improves the description of the semi-central and central CMS data [we will elaborate on the quantitative role of the B-meson resonance states in the $\Upsilon(2S)$ regeneration contribution in the next section]. The enhanced suppression of the $\Upsilon(1S)$, relative to the SBS, is welcome in comparison to the forward-rapidity ALICE data (lower panel of Fig. 14), although the latter are still significantly overpredicted.

To test the sensitivity of our results to a key in-medium property of the bottomonia, *i.e.*, their temperature-dependent binding energy as a measure of color screening, we additionally display in the upper panel of Fig. 14 the results of calculations where the baseline TBS binding energies are less (further) reduced, by decreasing (increasing) the in-medium reduction of E_B relative to the vacuum by 10 %; recall Eq. (3). This is implemented by changing the parameter η=1.0 to η=0.9 (η=1.1), displayed by the solid vs. dashed (dash-dotted) lines in Fig. 1 (recall that η=0 recovers the vacuum binding SBS). One finds a significant increase (decrease) of the inclusive $\Upsilon(1S)$ $R_{\rm AA}$, while the $\Upsilon(2S)$ $R_{\rm AA}$ is little affected [since $E_B(T)$ is already small]. Thus the inclusive $\Upsilon(1S)$ can in principle serve as a measure of color screening, provided other modeling uncertainties can be sufficiently controlled, as originally envisaged in Ref. [27]. In the following section, we will therefore scrutinize several of these uncertainties quantitatively. Since η=1.0 provides a compromise between the CMS and ALICE data, we adopt this value from hereon as our default (unless otherwise noted).

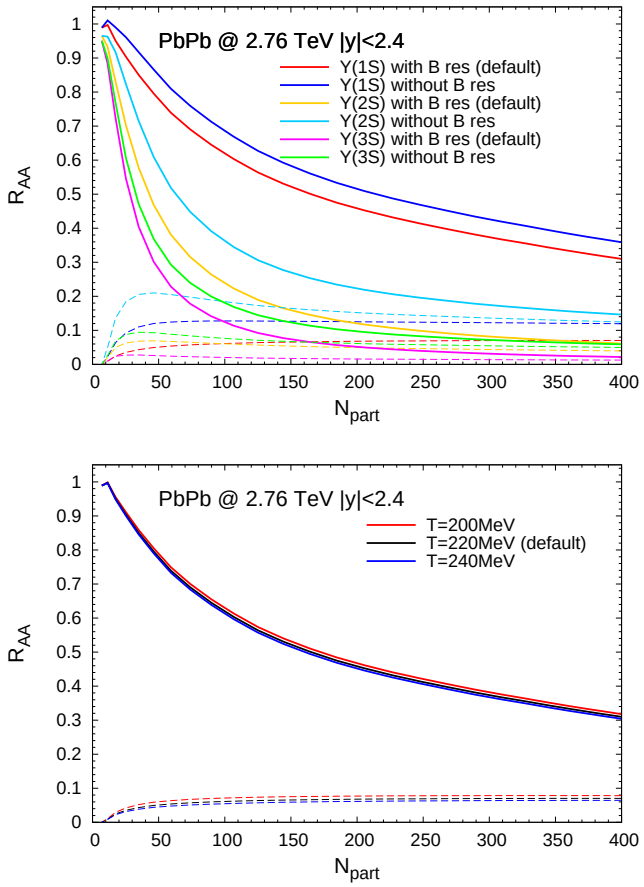

FIG. 15: Upper panel: comparison of $\Upsilon(1S)$, $\Upsilon(2S)$, and $\Upsilon(3S)$ $R_{\rm AA}$'s (solid lines: total; dashed lines: regeneration contribution) for the TBS with and without B-meson resonance states near $T_{\rm pc}$, assuming the default switching temperature of T=220 MeV. The red/blue curves are with/out resonances for $\Upsilon(1S)$, the cyan/yellow curve are with/out resonances for $\Upsilon(2S)$, and the magenta/green curves are with/out resonances for $\Upsilon(3S)$. Lower panel: sensitivity of the default scenario to the switching temperature.

C. Sensitivity to model parameters for TBS

This section is dedicated to quantify model dependencies unrelated to the in-medium binding energies of the bottomonium states. Specifically, we will quantify uncertainties in the implementation of the following components: (i) B-meson resonance formation, (ii) correlation volume, (iii) bottomonium formation time, (iv) QGP formation time, (v) fireball expansion, and (vi) b-quark relaxation time. We will discuss all these effects relative to our baseline TBS results (without shadowing), mostly focusing on (but not limited to) the centrality dependence of the $\Upsilon(1S)$ $R_{\rm AA}$ at mid-rapidity in Pb-Pb (2.76 TeV) collisions, with selected results also for the $\Upsilon(2S)$ and $\Upsilon(3S)$.

In the upper panel of Fig. 15 we display the comparison of total and regenerated contributions when switching off the presence of the B-meson resonance states in the calculation of the Y equilibrium limits near $T_{\rm pc}$ (recall Fig. 8). Without the resonance states, the b-quark fugacity factor is significantly larger in this temperature range, leading to an increase in the regeneration (while the primordial contribution is unaffected). The impact is most significant for the $\Upsilon(2S)$, where the regeneration contribution increases by close to a factor of 3 in central collisions. The effect is much less for the $\Upsilon(1S)$ (at $\sim$50%, translating into less than 20% for the total), since in the temperature range where the enhancement of the fugacity factor is active, the inelastic reaction rate of the $\Upsilon(1S)$ is already rather small, *e.g.*, $\Gamma_{\Upsilon(1S)} \lesssim 10$ MeV at T=220 MeV. For the $\Upsilon(3S)$ the increase of the regeneration component is also close to a factor of 3, but the absolute value of the regeneration contribution in the $R_{\rm AA}$ is smaller than for the $\Upsilon(2S)$ due to its larger mass (*i.e.*, smaller equilibrium limit). The relative enhancement of the regeneration components when neglecting B-meson resonance states is comparable at RHIC energy (not shown here), but overall less significant due to the generally larger primordial components compared

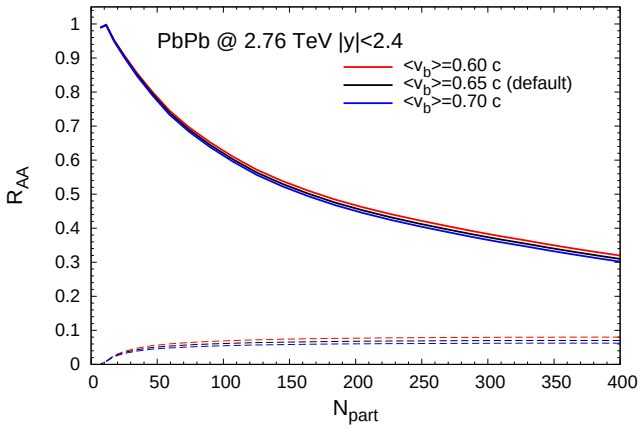

FIG. 16: Sensitivity of $\Upsilon(1S)$ production to the mean b-quark speed, $\langle v_b \rangle$, by which the correlation volume expands (red, black and blue lines are for $\langle v_b \rangle$=0.6c, 0.65c, and 0.7c, respectively). Solid (dashed) lines are for the total (regeneration component of the) $\Upsilon(1S)$ $R_{\rm AA}$ regeneration component

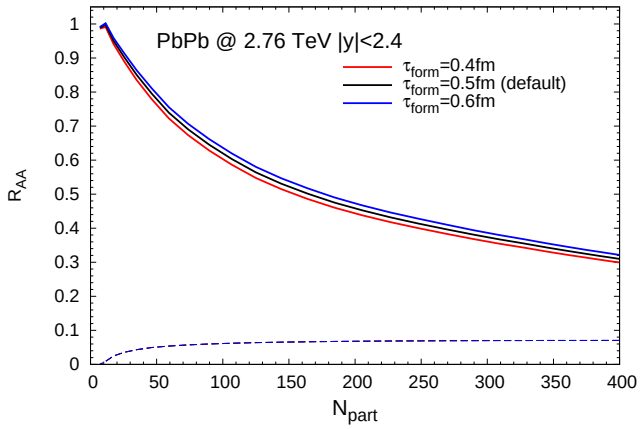

FIG. 17: Sensitivity of $\Upsilon(1S)$ production to a variation of the Y formation times by $\pm 20\,\%$.

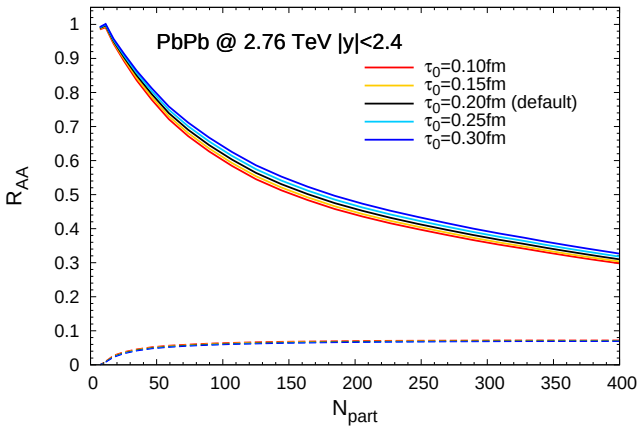

FIG. 18: Sensitivity of $\Upsilon(1S)$ production to a variation of the QGP formation time over the range τ_0=0.1-0.3 fm/c. The regeneration component (dashed lines) is virtually unaffected.

to 2.76 TeV.

We note that the calculations published in our recent papers [5, 65] did not yet include the B-meson resonance effects, which indeed led to problems with overestimating the $\Upsilon(2S)$ yields measured by CMS in semi-central and central Pb-Pb collisions at both 2.76 and 5.02 TeV. This problem is now largely resolved upon inclusion of this effect, which, as we mentioned above, is consistent with recent analysis of lQCD results for c-quark susceptibilities [43], and was predicted by T-matrix calculations with the U potential in Refs. [29, 66]. Thus, the qualitative feature of heavy-light resonances above $T_{\rm pc}$ is by now well established, but one still needs to further check its implementation. Toward this end we show in the lower panel of Fig. 15 the sensitivity of the $\Upsilon(1S)$ $R_{\rm AA}$ to the onset temperature assumed for the B-meson formation; it turns out to be small.

Second, we test the sensitivity to the modeling of the b-quark correlation volume, Eq. (9), by varying the mean speed, $\langle v_b \rangle$, with which the b and $\bar{b}$ quark expand the radius of the volume within which canonical (or "diagonal") regeneration can occur. A larger speed leads to a larger correlation volume which increases the available phase space for b quarks and thus decreases the b-quark fugacity, γ_b, and the pertinent regeneration yield. This model component creates a small uncertainty in the $\Upsilon(1S)$ $R_{\rm AA}$; cf. Fig. 16.

Third, we test the sensitivity to the formation times, $\tau_{\rm form}$, of the Y states, by varying the default values of 0.5, 1.0 and 1.5 fm for $\Upsilon(1S)$, $\Upsilon(2S)$, and $\Upsilon(3S)$, respectively, by $\pm 20\,\%$. Larger formation times reduce the dissociation rates in the early stages thus resulting in less suppression of the primordial component. This is mostly relevant for the $\Upsilon(1S)$ whose suppression has the largest sensitivity to the earliest phases. However, the pertinent variation of its total $R_{\rm AA}$ is below 5%; cf. Fig. 17.

Fourth, we test the sensitivity to the initial QGP formation time, τ_0, which controls the initial temperature, T_0. Varying τ_0 by ± 0.1 fm around the default value of 0.2 fm, which implies a formidable range of initial temperatures of $T_0 \simeq$520-750 MeV, produces relatively small modifications in the $\Upsilon(1S)$ $R_{\rm AA}$; cf. Fig. 18. One of the reasons for this is that the $\Upsilon(1S)$ formation times "protect" it from large dissociation rates in the earliest phase of the medium evolution. Another reason is that, despite the large range in temperature, the variation in the absolute time duration is actually rather small (since the default value is already quite small), so that even rather large widths do not have a strong impact. This further implies that pre-equilibrium evolution also has a small effect on the Y production yields.

Fifth, we have checked the sensitivity to the fireball expansion parametrization, Eq. (12). When increasing

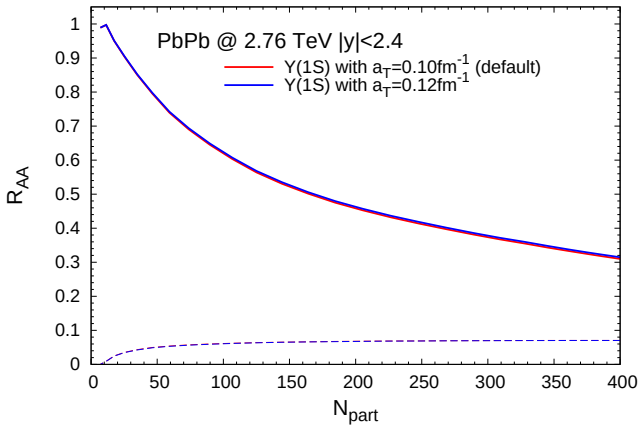

FIG. 19: Sensitivity of $\Upsilon(1S)$ production to a variation of the fireball expansion acceleration over the range $a_{\rm T}$=0.10-0.12 /fm.

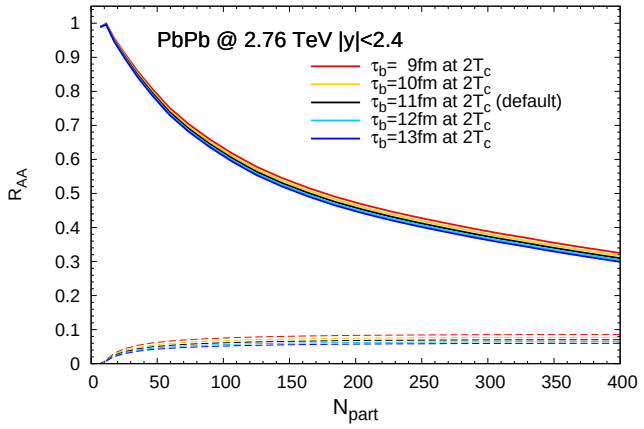

FIG. 20: Sensitivity of $\Upsilon(1S)$ production to the b-quark thermalization time, τ_b, over the range τ_b=8-12 fm at $2T_{\rm pc}$. Dashed lines are for the regeneration component.

the transverse acceleration by 20%, from a_T=0.1/fm to 0.12/fm, both the regeneration contribution and the total $\Upsilon(1S)$ $R_{\rm AA}$ change by no more than within the typical line thickness of the baseline curves; cf. Fig. 19.

Sixth, we vary the thermal relaxation time of b quarks, τ_b, which controls the time scale for approaching the Y equilibrium limits. Larger relaxation times cause the equilibrium limits to be recovered slower which reduces the regeneration contributions; recall Eq. (11) for the explicit expression of this implementation. The thermal relaxation time of heavy quarks is one of the key transport parameters in URHICs, being proportional to the spatial heavy-quark diffusion coefficient via $\mathcal{D}_s = \tau_Q(T/m_Q)$. Intense efforts are ongoing to extract this quantity from open heavy-flavor observables, *i.e.*, from D-meson $R_{\rm AA}$'s and v_2's, or, in the future, and more directly related to the present context, from B-meson observables. Our default choice of τ_b=11 fm at a "pivot point" of $2\,T_{\rm c}$, with

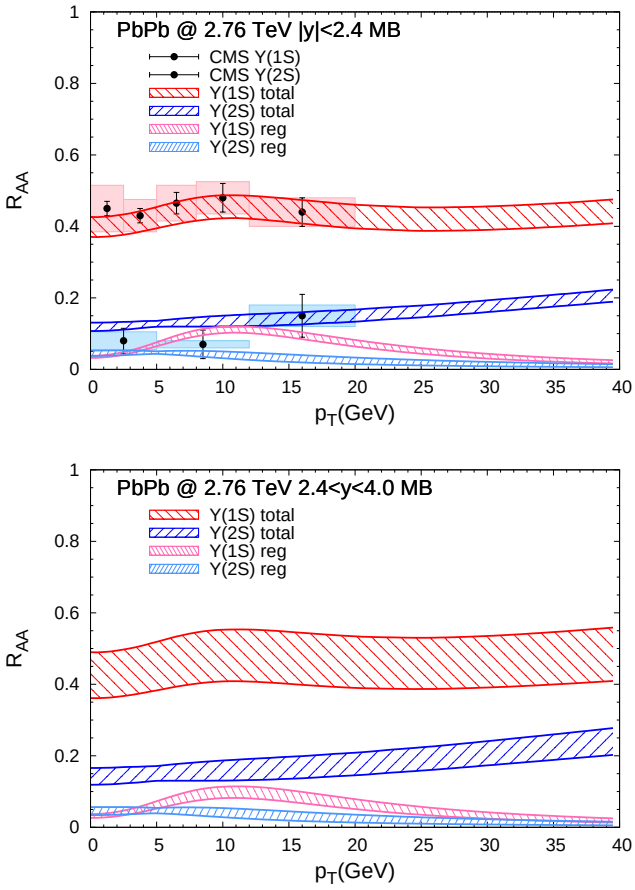

FIG. 21: Transverse-momentum dependent $R_{\rm AA}$ for inclusive $\Upsilon(1S)$ (red band) and $\Upsilon(2S)$ (blue band) production and their regeneration component (pink and light blue bands, respectively) in minimum-bias Pb-Pb(2.76 TeV) collisions within the TBS for η=1.0 at mid- and forward rapidity (upper and lower panel, respectively), compared to CMS data [31]. The width of the total bands includes a 0-15% (0-30%) shadowing suppression for $|y| < 2.4$ ($2.5 < y < 4.0$), the variation in the temperature window for the regeneration component (also shown separately) and the uncertainty in the pp baseline spectra.

a mild temperature dependence, approximately reflects our current knowledge of this quantity (cf. Ref. [67] for a recent review). Not unexpectedly, the regeneration contribution to the $\Upsilon(1S)$ $R_{\rm AA}$ varies by almost ±20% when varying this parameter by ±20%; see Fig. 20. However, the relative variation in the total $\Upsilon(1S)$ $R_{\rm AA}$ is much smaller, within ±5%. Future analysis of open-bottom observables to extract the temperature-dependent bottom diffusion coefficient in the QGP will help to reduce this uncertainty.

D. Transverse-momentum dependence for TBS

For the pp baseline spectra, which figure into the denominator of the $R_{\rm AA}(p_T)$, we use the same expression,

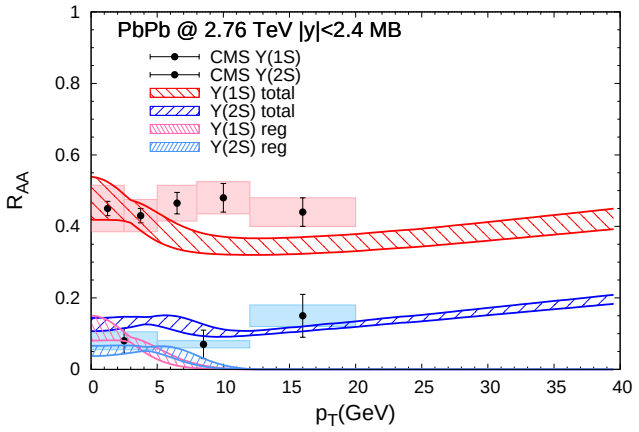

FIG. 22: Same as upper panel in Fig. 21 but with the regeneration component evaluated by a thermal blast-wave approximation for the respective Y states.

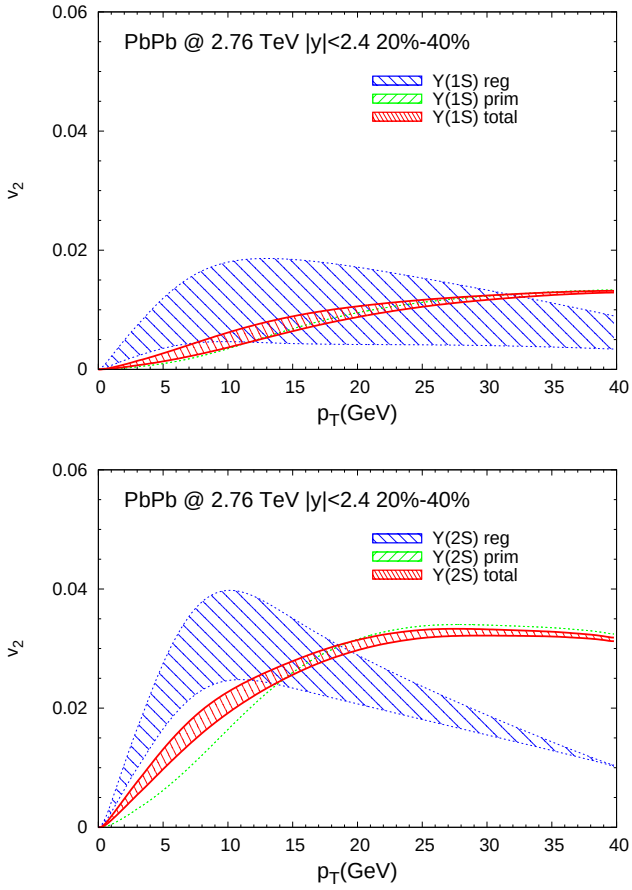

FIG. 23: The p_T dependence of elliptic flow of $\Upsilon(1S)$ (upper panel) and $\Upsilon(2S)$ (lower panel) in semi-central Pb-Pb(2.76 TeV) at mid-rapidity within the TBS (η=1.0). In both panels the blue, green, and red curves are for the regeneration component, primordial component and their weighted sum, respectively, where the band widths reflect uncertainties from varying the average regeneration temperatures.

Eq. (33), as given in Sec. III B, but with parameters A=3.0 (3.0), D=5.8 (6.6) GeV refitted to $\Upsilon(1S)$ ($\Upsilon(2S)$) spectra at 2.76 TeV, as well as A=2.3 (2.3) and D=4.9 (5.9) GeV at 5.02 TeV [68–72].

To compute the coalescence component, a temperature range for the hydro hypersurface has to be specified to evaluate the b-quark spectra from the Langevin simulations in the hydrodynamic background. This range represents the window over which most of the regeneration of the corresponding bottomonium state occurs. Inspection of the time (temperature) evolution of the regeneration yields reveals that the relevant temperature windows are $\bar{T}_{\rm reg}$=220-278 MeV for the $\Upsilon(1S)$, $\bar{T}_{\rm reg}$=183-201 MeV for the $\Upsilon(2S)$ and $\bar{T}_{\rm reg}$=189-212 MeV for the χ_b states in minimum-bias (MB) Pb-Pb (2.76 TeV) collisions. We use the upper and lower limits of these windows to define the uncertainty band for the p_T spectra of the regenerated bottomonia.

The resulting $R_{\rm AA}(p_T)$'s for $\Upsilon(1S)$ and $\Upsilon(2S)$ are displayed in Fig. 21 for the TBS with η=1.0. The interplay of primordial suppression and coalescence processes results in a total $\Upsilon(1S)$ $R_{\rm AA}$'s with a mild maximum structure around $p_T \simeq m_{\Upsilon(1S)}$, caused by the regeneration contribution, in approximate agreement with CMS data [31]. For the $\Upsilon(2S)$, we find an over-prediction at low p_T, which is not really apparent in the centrality-dependent $R_{\rm AA}(N_{\rm part})$ in Fig. 14. However, when instead replacing the regeneration contribution with a thermal blast-wave expression (corresponding to thermally equilibrated b-quark distributions), the low-p_T maximum structure in the $R_{\rm AA}(p_T)$ becomes more pronounced and leads to larger deviations from the CMS data, see Fig. 22. It thus appears that kinetically not equilibrated b-quark spectra are an important ingredient to properly interpret the bottomonium p_T spectra.

E. Elliptic flow for TBS

Based on the bottomonium p_T spectra discussed in the previous section, we provide our predictions for their elliptic flow within the framework laid out in Sec. II C 3; see Fig. 23. The same sources of uncertainties apply as encoded in the bands for the p_T spectra. The resulting $\Upsilon(1S)$ v_2 turns out to be a factor of 2-3 smaller than the one of the $\Upsilon(2S)$. However, this is not due to the larger relative contribution of the coalescence yields, since the latter affects the total weighted v_2 for both particles very little: for the $\Upsilon(1S)$ the coalescence contribution has almost no effect on the total v_2, while for the $\Upsilon(2S)$ it increases the total relative to the primordial by up to a maximum of 1% at low $p_T \simeq$5 GeV, where, however, the total v_2 signal is not even at 2%. Thus, at our predicted level of coalescence contributions, and due to their concentration at low p_T where the absolute signal is small, we conclude that it will be very challenging at best to

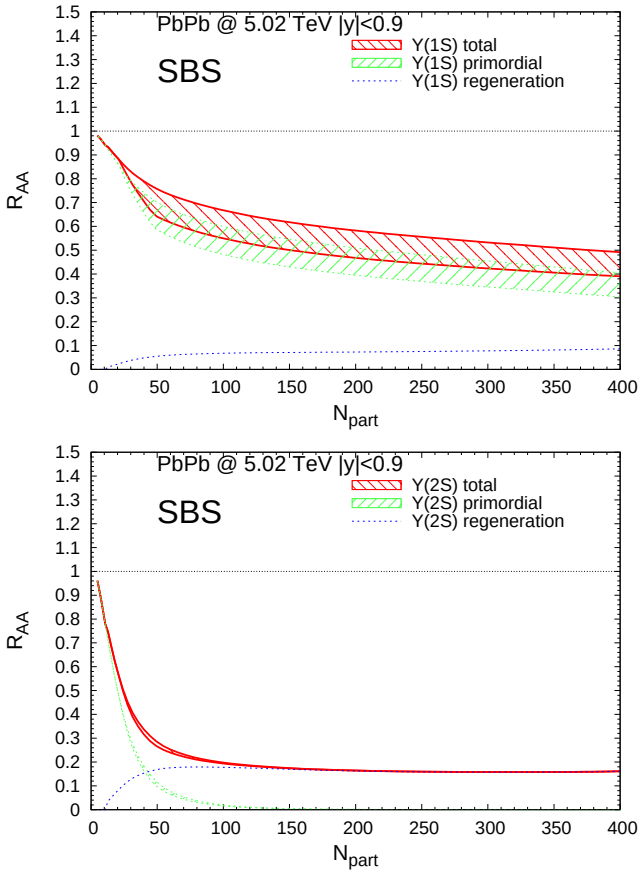

FIG. 24: Centrality dependence of $R_{\rm AA}$ for $\Upsilon(1S)$ (upper panel) and $\Upsilon(2S)$ (lower panel) within the SBS in Pb-Pb(5.02 TeV) collisions at mid-rapidity. Red, green and blue lines represent the total, primordial and regeneration contributions, where the bands reflect a 0-25% shadowing effect.

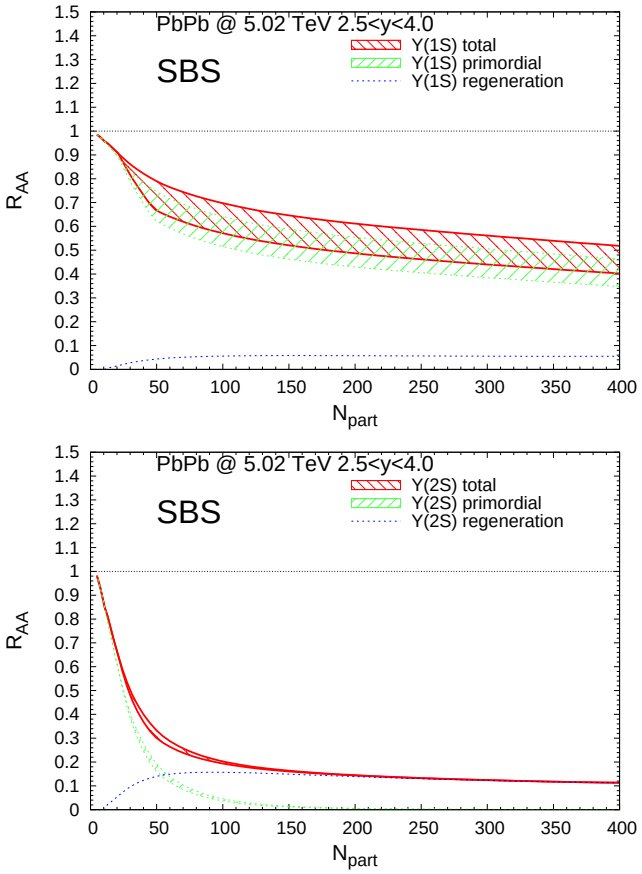

FIG. 25: Same as Fig. 24 but at forward rapidity.

discern them from the primordial contributions. On the other hand, the significantly larger *total* v_2 of the $\Upsilon(2S)$ compared to the $\Upsilon(1S)$ is a more robust signal; it is due to the fact that the $\Upsilon(1S)$ suppression occurs earlier in the fireball evolution, where path length differences in the suppression cannot be sensed as much as they can for the $\Upsilon(2S)$ where the suppression mechanism is active to lower temperatures, *i.e.*, later in the fireball evolution. In other words, a temperature-sequential suppression, which is widely believed to be at the origin of the difference of the $\Upsilon(1S)$ and $\Upsilon(2S)$ yields, should also manifest itself as a difference in their v_2, irrespective of regeneration.

V. BOTTOMONIUM PRODUCTION IN 5.02 TEV PB-PB COLLISIONS

We now turn to Pb-Pb collisions at 5.02 TeV which were recently conducted at the LHC., Several new bottomonium data from this run have already become available over the course the present work, and we include those in our discussion. For the fireball evolution, we have assumed the charged-particle rapidity density, $\frac{{\rm d}N_{ch}}{{\rm d}y}$, to increase by about 22.5 %, from 2.76 to 5.02 TeV, *e.g.*, from 1750 to 2150 in 0-5% central collisions [73]. This corresponds to an increase of the total entropy in the fireball from 22000 to almost 27000. With an entropy density of $s \sim T^3$ in the early hot phases, the initial temperature increases by about 7%. For the charged-particle rapidity density we implement a reduction of 20 % from mid-rapidity, $|y| < 2.4$, to forward rapidity, $2.5 < y < 4.0$ [74], as previously done at 2.76 TeV. We will start our discussion again by recalling the results from the earlier used SBS in Sec. V A, and then turn to the centrality, p_T, and azimuthal-angle dependencies for the default TBS in Sec. V B.

A. Centrality Dependence for SBS

We first display our 5.02 TeV results for Y production in the previously used SBS [28] with updated feeddown fractions (but without explicit treatment of the $3S$ or $2P$ states), at both mid- and forward rapidities, cf. Figs. 24 and 25, respectively. Compared to the SBS results at

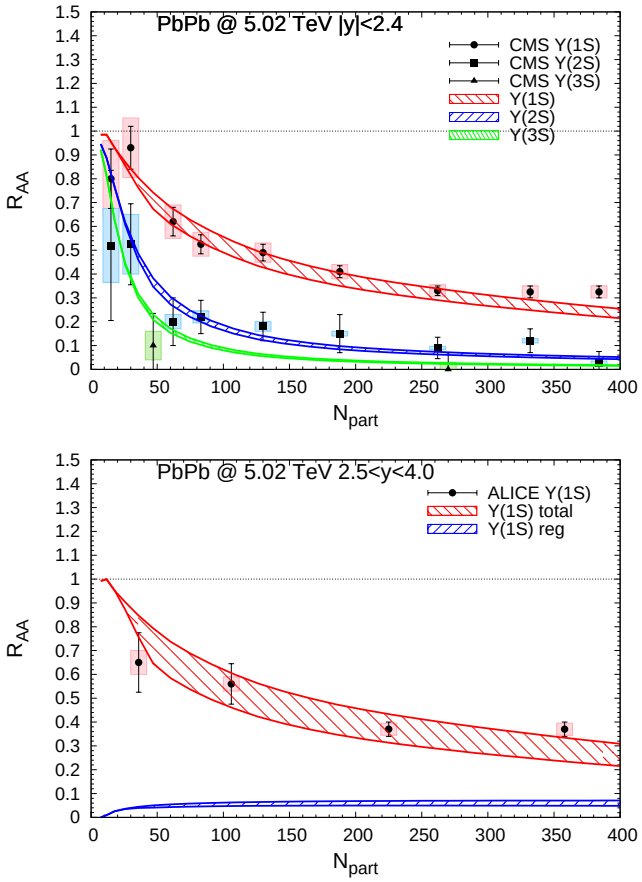

FIG. 26: Centrality dependence of bottomonium $R_{\rm AA}$'s in Pb-Pb(5.02 TeV) collisions within the TBS (η=1.0). Upper panel: mid-rapidity $\Upsilon(1S)$, $\Upsilon(2S)$ and $\Upsilon(3S)$ (red, blue and green bands, respectively) compared to CMS data [59, 60]; the bands are due to a 0-15% shadowing suppression. Lower panel: forward rapidity $\Upsilon(1S)$ compared to ALICE data [75, 76]; the bands are due to a 0-30% shadowing suppression.

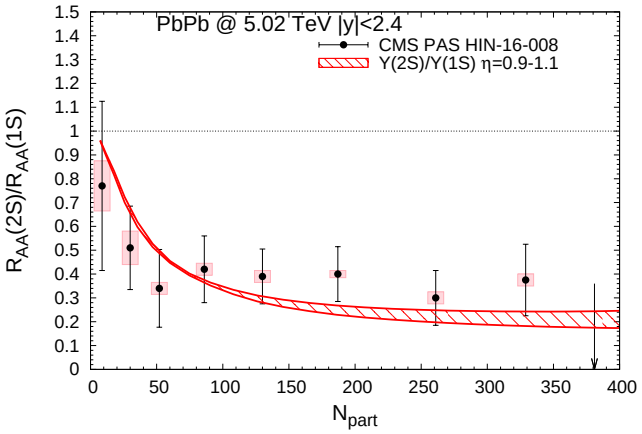

FIG. 27: Centrality dependence of the $\Upsilon(2S)/\Upsilon(1S)$ $R_{\rm AA}$ double ratio in 5.02 TeV Pb-Pb collisions at mid-rapidity within the TBS (with an uncertainty band from in-medium binding energies for η=0.9-1.1), compared to CMS data [77].

2.76 TeV, the $\Upsilon(1S)$ suppression slightly increases by up to ∼5% in central collisions, due to stronger color screening with increased rates at higher temperature. On the other hand, the $\Upsilon(2S)$ suppression becomes slightly less in central collisions at 5.02 TeV due to a small increase in regeneration, while a stronger suppression is found for peripheral collisions ($N_{\rm part} \lesssim 50$), where the suppressed primordial contribution dominates (again for both rapidity regions). This feature is reminiscent of the J/ψ case.

B. Centrality and transverse-momentum dependence for TBS

Next, we turn to the TBS at 5.02 TeV, encoding our theoretical improvements in the Y transport approach over the previously used SBS. The centrality dependence of the $R_{\rm AA}$ for $\Upsilon(1S)$ and $\Upsilon(2S)$ at mid-rapidity is shown in the upper panel of Fig. 26, and for the $\Upsilon(1S)$ at forward rapidity in the lower panel of Fig. 26. They are compared to CMS data [59, 60] at mid-rapidity and to ALICE data [75, 76] at forward rapidity, respectively. The in-medium effects lead to a significantly stronger suppression of the $\Upsilon(1S)$ relative to the SBS discussed in the previous section. At the same time, the $\Upsilon(1S)$ suppression within the TBS is only slightly increased relative to the 2.76 TeV results (recall Fig. 14). The $\Upsilon(2S)$ $R_{\rm AA}$ also shows a small increase in suppression by about 15%, amounting, however, to only a ∼0.01 change at the absolute level in the $R_{\rm AA}$ in central collisions. For the latter, the $\Upsilon(3S)$ is suppressed by another factor of ∼2. At forward rapidity, the comparison to recent ALICE data [75, 76], shown in the lower panel of Fig. 26, is more favorable than it was at 2.76 TeV.

Next, we compare our calculations for the $\Upsilon(2S)$-over-$\Upsilon(1S)$ double ratio at 5.02 TeV to CMS data [77] in Fig. 27; as to be expected from the agreement with the individual $R_{\rm AA}$'s, the calculated double ratio also agrees fairly well with the observed centrality dependence.

Finally, we extract transverse-momentum dependent observables from our calculations, starting with the p_T dependence of the $R_{\rm AA}$ for $\Upsilon(1S)$ and $\Upsilon(2S)$ at mid- and forward rapidities; cf. Fig. 28. Similar to what we found at 2.76 TeV, the $\Upsilon(1S)$ $R_{\rm AA}(p_T)$ exhibits a mild maximum structure due to the regeneration contribution computed with non-thermalized b-quark spectra (taken from Langevin transport calculations at 5.02 TeV), at both mid- and forward rapidities. The calculations approximately agree with both CMS data at mid-rapidity (upper panel of Fig. 28) and ALICE data at forward rapidity (middle panel of Fig. 28). The $\Upsilon(2S)$ $R_{\rm AA}(p_T)$ is also similar to 2.76 TeV, with a moderate monotonous rise with p_T. The absolute magnitude of the calculated p_T spectra agrees better with the CMS data than at 2.76 TeV. We also plot the p_T-dependent double ratio at mid-rapidity in the lower panel of Fig. 28; again, based on the agreement with the individual $R_{\rm AA}(p_T)$'s in the

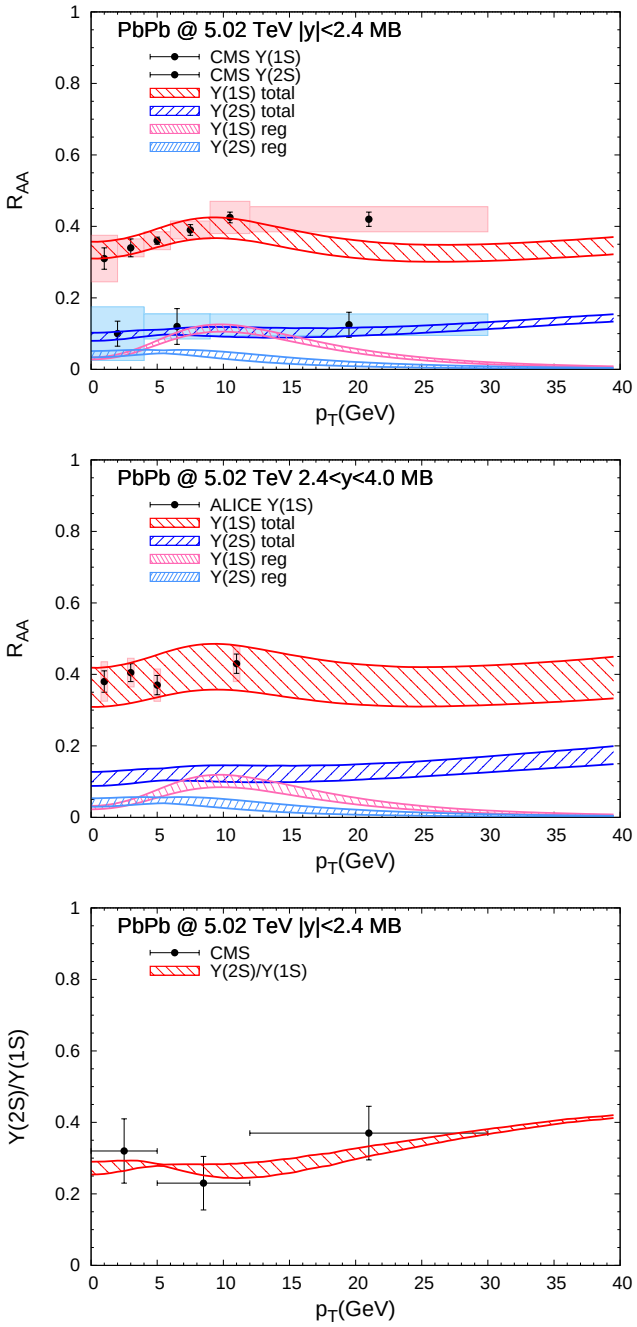

FIG. 28: The p_T dependence of $\Upsilon(1S)$ and $\Upsilon(2S)$ yields in MB Pb-Pb(5.02 TeV) collisions at mid and forward rapidities within the TBS (η=1.0). Upper panel: mid-rapidity $\Upsilon(1S)$ and $\Upsilon(2S)$ $R_{\rm AA}$ for total (red and blue curves, respectively) and regeneration components (pink and light-blue curves, respectively), compared to CMS data [59, 60]; the bands reflect variations due to a 0-15% shadowing suppression and the average regeneration temperatures ($\bar{T}_{\rm reg}$) of the two states. Middle panel: same as upper panel but at forward rapidity with a 0-30% shadowing range, compared to ALICE data [76]. Lower panel: $\Upsilon(2S)/\Upsilon(1S)$ $R_{\rm AA}$ double ratio compared to CMS data [77]; the band reflects variations in the $\bar{T}_{\rm reg}$'s.

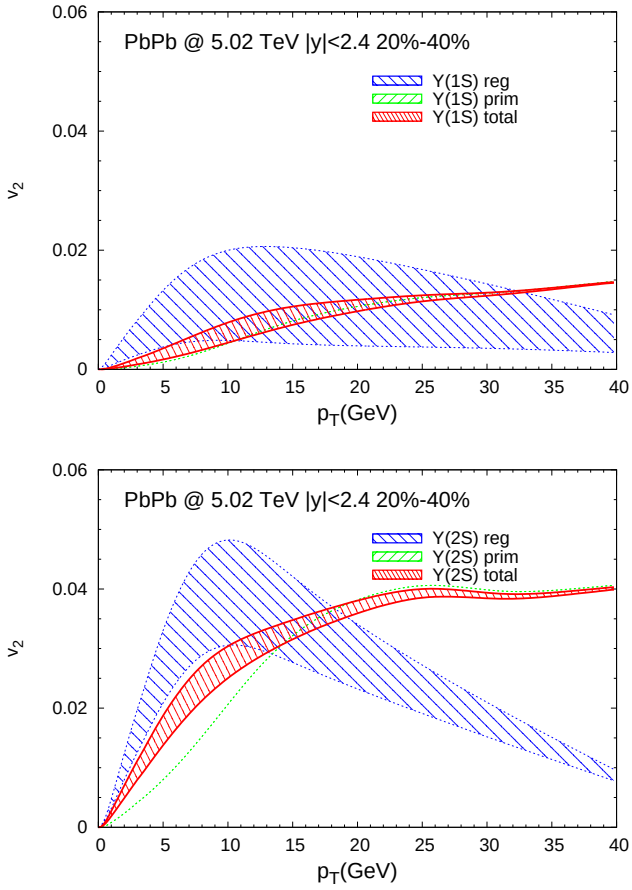

FIG. 29: The p_T dependence of elliptic flow of $\Upsilon(1S)$ (upper panel) and $\Upsilon(2S)$ (lower panel) in semi-central Pb-Pb(5.02 TeV) at mid-rapidity within the TBS (η=1.0). In both panels the blue, green, and red curves are for the regeneration component, primordial component, and their weighted sum, respectively, where the band widths reflect uncertainties from varying the average regeneration temperatures.

upper panel, no surprises are found.

The p_T dependence of the elliptic flow for $\Upsilon(1S)$ and $\Upsilon(2S)$ in mid-central Pb-Pb collisions at mid-rapidity is displayed in Fig. 29. The v_2 for both the primordial and regenerated $\Upsilon(1S)$ are small, below 2%, since both processes occur early in the fireball evolution – essentially within the first 2fm/c – during which both path length differences and collective-flow anisotropies are limited. The v_2 is more than doubled for the $\Upsilon(2S)$ in both components, which, after an initial rise, levels off at about 4%. As was the case at 2.76 TeV, the v_2 does not show a very promising sensitivity to the regeneration component, since the latter is rather small and concentrated at low p_T, where the mass effect suppresses the signal. However, the difference between $\Upsilon(1S)$ and $\Upsilon(2S)$ v_2's is appreciable; about a factor of $\sim$2. We note that we did not include initial geometry fluctuations nor elastic rescattering of the Y states in the medium (once they are reasonably tightly bound), which may play a role in

generating a larger v_2 of the primordial component at high p_T or the total yields at small and moderate p_T, respectively.

VI. EXCITATION FUNCTION

In an attempt to combine the information attained within our updated TBS approach to Y production from RHIC to top LHC energy, we compare our results for the collision energy dependence of the minimum-bias (MB) $R_{\rm AA}$'s for $\Upsilon(1S)$ and $\Upsilon(2S)$ to STAR and CMS data at mid-rapidity in Fig. 30. We find a gradual increase in the suppression for both states, with a stronger absolute suppression of the $\Upsilon(2S)$ than the $\Upsilon(1S)$ especially at the LHC. These features support a sequential suppression scenario, rather directly reflected in both calculations and data due to relatively small regeneration contributions. The latter is due to a combination of the small $b\bar{b}$ cross section (which at current energies does not produce more than 1 pair per fireball) and the role played by B-meson resonance formation near $T_{\rm pc}$. The possibly most significant indication for the regeneration contribution is a hint for a flattening of the $\Upsilon(2S)$ $R_{\rm AA}(\sqrt{s})$ when going from 2.76 to 5.02 TeV, in both data and calculations. The slight increase in the $\Upsilon(1S)$ regeneration, which is subleading at current energies, is expected to become more significant at collision energies beyond ∼10 TeV.

As pointed out in Ref. [5], the decreasing Y excitation functions are markedly different from their J/ψ counterparts, despite the comparable [or even larger] binding energy of the $\Upsilon(2S)$ [$\Upsilon(1S)$]. This lends considerable support to the overall picture of quarkonium kinetics developed over the last decade. The relatively large uncertainty in the CNM effects at RHIC clearly calls for an improved measurement in p-A d-A collisions at these energies (interesting effects have also been observed in p-Pb at the LHC [6, 62–64, 78]). At face value, the $\Upsilon(1S)$ suppression measured by STAR in Au-Au ($\sqrt{s}$=0.2 TeV), which is very similar to the LHC datum at 2.76 TeV, is not easily understood from hot-medium effects alone, while a larger CNM absorption at RHIC could offer a natural explanation for this observation. An analogous situation is present for the J/ψ, where the larger CNM suppression at the lower SPS energies ($\sqrt{s}$=0.017 TeV), relative to RHIC, is an important ingredient to interpret the energy dependence of the hot-medium effects [5]. In addition, a more precise measurement of the Y excited states at RHIC would go a long way in improving estimates of the $\Upsilon(2S)$ and $\Upsilon(3S)$ dissociation energies.

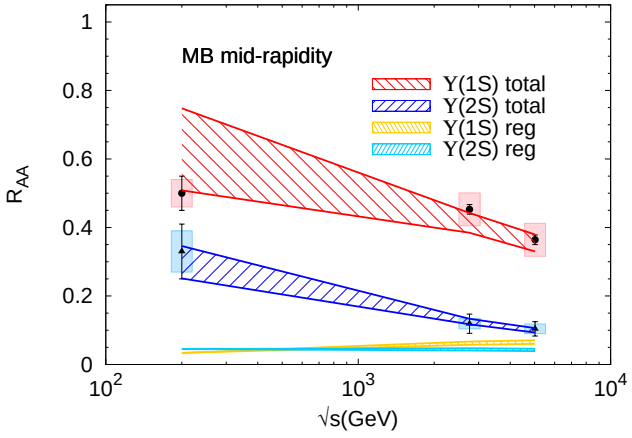

FIG. 30: Excitation function the MB $R_{\rm AA}$ of $\Upsilon(1S)$ and $\Upsilon(2S)$ with TBS compared to STAR [54] and CMS [31, 59, 60] data at mid-rapidity.

VII. CONCLUSIONS

In the present work we have refined our previous Boltzmann/rate-equation approach to bottomonium transport in heavy-ion collisions. The improvements include the use of in-medium binding energies and their consequences for dissociation mechanisms and pertinent rates, a lQCD-based equation of state for the fireball evolution, correlation volume effects for regeneration reactions, and B-meson resonance states appearing close to T_{pc} affecting the regeneration transport parameter. In this way, the approach has been brought to the same level as employed before for charmonia, and thus enables interpretations of bottomonium data on an equal footing. In particular, the role of regeneration contributions, which are essential for charmonia at the LHC, is a priori less obvious for bottomonia. In an attempt to augment possible signatures of those, we extended our calculations of the centrality dependence of inclusive bottomonium yields to transverse-momentum spectra and elliptic flow.

Overall, our improved approach allows for a fair description of existing $\Upsilon(1S)$, $\Upsilon(2S)$ and $\Upsilon(3S)$ observables at RHIC and the LHC, including new data released from both facilities very recently. We have found that the suppression level of the $\Upsilon(1S)$ $R_{\rm AA}$ at the LHC has a significant sensitivity to the in-medium binding energy used in the calculations and thus can, in principle, serve as a quantitative measure of the screening of the heavy-quark potential in the QGP. A similar sensitivity at RHIC energies requires a better control over the CNM effects. At this point, the LHC data suggest a rather strong heavy-quark potential which supports $\Upsilon(1S)$ states out to temperatures of $T\simeq$500 MeV. Inelastic reaction rates can, of course, break up $\Upsilon(1S)$ states at temperatures well below that. The strong suppression of the $\Upsilon(2S)$, on the other hand, suggests its melting at much lower temperatures, around $T\simeq$240 MeV, implying strong screening effects on the linear ("confining") part of the heavy-quark potential in this regime. We also found that the emergence of B-mesons near $T_{\rm pc}$, which lowers the equilibrium limit of the Y states, reduces the regeneration of the $\Upsilon(2S)$, which helps in quantitatively describing the pertinent CMS data at both 2.76 and 5.02 TeV. Some

tension persists between our results and the forward-rapidity $\Upsilon(1S)$ ALICE data in Pb-Pb(2.76 TeV) collisions, which show a stronger suppression than obtained from our calculations. The regeneration contributions for both $\Upsilon(1S)$ and $\Upsilon(2S)$ come out at a rather generic level of around $R_{\rm AA}\simeq 0.05$-0.1 [smaller for the $\Upsilon(3S)$], across centrality (for $N_{\rm part}\gtrsim 100$), rapidity and collision energy (even down to RHIC energies). This is mostly a consequence of the canonical limit, *i.e.*, small open-bottom cross sections which limit the number of $b\bar{b}$ pairs to either zero or one in a given fireball. In the calculations of transverse-momentum spectra, the 3-momentum dependence of the dissociation rates tends to produce a decrease of the primordial $R_{\rm AA}(p_T)$, which, however, is counter-balanced by formation time effects at high p_T. For the regeneration component, the inclusion of realistic b-quark spectra, taken from Langevin transport simulations which do not kinetically equilibrate, turns out to be significant. Even though the coalescence contribution is not large, a thermal blast-wave approximation for regenerated bottomonia produces a low-p_T enhancement in the $R_{\rm AA}(p_T)$ which is disfavored by the CMS data (in contrast to the J/ψ case, where a marked low-p_T enhancement is observed). On the other hand, using the transport b-quark spectra, the regeneration component generates a mild maximum structure in the $\Upsilon(1S)$ $R_{\rm AA}(p_T)$ around $p_T\lesssim 10\,$GeV, which is consistent with experiment. Our predictions for Y elliptic flow do not exhibit significant discrimination power between primordial and regeneration mechanisms. However, we predict a factor of $\sim$2 larger total v_2 for the $\Upsilon(2S)$ than for the $\Upsilon(1S)$, since the inelastic reactions for the former remain active to lower temperatures. This should be helpful in either refuting or corroborating the sequential melting and regeneration, as opposed to, *e.g.*, statistical production of both particles at the same temperature.

Future work should focus on improving the precision of the approach on several fronts. Our initial checks of various model components (pertaining to the bulk evolution, correlation volume, Y formation time and b-quark thermalization) indicate a promising robustness of our results, in particular with regards to connecting the observed level of $\Upsilon(1S)$ suppression to the screening of the fundamental QCD force in the QGP. However, the interplay of the early bulk medium evolution with quantum effects in the $b\bar{b}$ wave package deserves further studies [79–82]. This also applies to nonperturbative interactions in the Y dissociation mechanisms (*e.g.*, by using explicit T-matrix interactions), which, after all, play a central role in understanding the strong coupling of individual heavy quarks diffusing through the QGP. These developments will improve our understanding of the systematic errors in the present results and enable a more controlled assessment of the modifications of the fundamental QCD force in the QGP.

Acknowledgments

We thank X. Zhao and A. Emerick for helpful discussions, and J. Fox for his contributions in the early stages of this work. This work has been supported by the U.S. National Science Foundation under Grant No. PHY-1614484. M. He was supported by NSFC Grant No. 11675079.

Appendix A: Inelastic Bottomonium Cross Sections

In this appendix we briefly recollect the expressions used for the cross sections for the inelastic bottomonium reactions with quarks and gluons.

For gluo-dissociation, $g+Y\to b+\bar{b}$, we employ the cross sections derived from the operator product expansion for a Coulombic bound state by Bhanot and Peskin [39],

$$\sigma_{Yg\to b\bar{b}}=\frac{r_0}{m_b}g_Y(x) \tag{A1}$$

where r_0 is the ground-state radius and

$$g_Y(x)=\begin{cases}\frac{2}{3}\pi\left(\frac{32}{3}\right)^2\frac{(x-1)^{\frac{3}{2}}}{x^5} & \text{for } \Upsilon(1S)\\ \frac{2}{3}\pi\left(\frac{32}{3}\right)^2\frac{16(x-1)^{\frac{3}{2}}(x-3)^2}{x^7} & \text{for } \Upsilon(2S)\\ \frac{2}{3}\pi\left(\frac{32}{3}\right)^2\frac{4(x-1)^{\frac{1}{2}}\left(9x^2-20x+12\right)}{x^7} & \text{for } \chi(1P)\end{cases} \tag{A2}$$

where $x=k_0/E_B$ and $k_0=\frac{s-m_Y^2-m_g^2}{2m_Y}$ is the incident gluon energy in the quarkonium for a center-of-mass energy squared:

$$s=(p_Y^{(4)}+p_g^{(4)})^2=m_Y^2+m_g^2+2\omega_Y\omega_g-2\vec{p}_Y\cdot\vec{p}_g\ ; \tag{A3}$$

$p_Y^{(4)}=(\omega_Y,\vec{p}_Y)$ and $p_g^{(4)}=(\omega_g,\vec{p}_g)$ denote the 4-momenta of the incoming bottomonium and outgoing gluon, respectively. The color-Coulomb binding energy and radius follow the hydrogen form,

$$E_0 = \left(\frac{N^2-1}{2N}\alpha_s\right)^2\frac{m_b}{4}=\left(\frac{2\alpha_s}{3}\right)^2 m_b \tag{A4}$$

$$r_0 = \frac{2}{m_b\alpha_s}\left(\frac{2N}{N^2-1}\right)=\frac{3}{2m_b\alpha_s} \tag{A5}$$

which slightly differs from the large-N_c limit expressions

$$E_0 = \left(\frac{N}{2}\alpha_s\right)^2\frac{m_b}{4}=\left(\frac{3\alpha_s}{4}\right)^2 m_b \tag{A6}$$

$$r_0 = \frac{2}{m_b\alpha_s}\left(\frac{2}{N}\right)=\frac{4}{3m_b\alpha_s} \tag{A7}$$

underlying the coefficients in Eq. (A2).

In previous work [28], the binding energies in the SBS were taken at the vacuum values defined by $E_B = 2m_B - m_Y = 1.1[0.54]\,\mathrm{GeV}$ for the $\Upsilon(1S)$ $[\Upsilon(2S)]$ with the coupling constant fixed via the ground-state expression, Eq. (A4). We here adopt an alternative treatment, which we believe to be more realistic, by eliminating the r_0 dependence and rewriting the cross section as the first power in α_s times a factor involving the binding energies using the relation of the bottomonium radius to their binding energies from the hydrogen model expression. With $\sigma \sim \frac{r_0}{m_b} \sim \alpha_s \cdot r_0^2 \sim \frac{\alpha_s}{m_b E_B}$, the cross sections become

$$\sigma_{Y g\to b\bar{b}} = \frac{2\alpha_s}{3 m_b E_0} g_Y(x) \tag{A8}$$

Since the in-medium binding energies of the Y states are not necessarily small compared to the temperature, we also include a phenomenological treatment of interference effects for the quasifree reaction rates. Starting from the original expression for the quasifree cross section, schematically given by $\sigma_{Y p\to b\bar{b}p}(s) \simeq \int \frac{\mathrm{d}\sigma_{Y p\to b\bar{b}p}(s,t,u)}{\mathrm{d}t}\mathrm{d}t$, (which includes the t-channel from both quark and gluon as partons, s- and u-channels from gluon as parton, and their mixed terms) the interference correction is implemented as

$$\sigma_{Y p\to b\bar{b}p}(s) \simeq \int \mathrm{d}t \left(\frac{\mathrm{d}\sigma_{Y p\to b\bar{b}p}(s,t,u)}{\mathrm{d}t}\right) \times \left(1 - \frac{\sin(\sqrt{-t}r)}{\sqrt{-t}r}\right) \tag{A9}$$

(which also influences the p_T dependence). To relate the dependence on the coordinate r to the in-medium binding energy, E_B, we utilize the Coulomb relations for the two scales $p \sim m_b\alpha_s \sim \frac{1}{r}$ and $E_B \sim m_b\alpha_s^2$. One can then either re-express the mass or coupling constant leading to $E_B \sim \frac{\alpha_s}{r}$ or $E_B \sim \frac{1}{m_b r^2}$, respectively. To check which relation is more realistic, especially in the presence of the nonperturbative string term, we determine the numerical coefficients for each option from the vacuum binding energy and radius of the $\Upsilon(1S)$ and then inspect the pertinent prediction for the $\Upsilon(2S)$. With $\alpha_s{\simeq}0.3$, $m_b{\simeq}5\,\mathrm{GeV}$ and a vacuum binding and radius of $E_B(\Upsilon(1S)){\simeq}1\,\mathrm{GeV}$ and $r(\Upsilon(1S)){\simeq}0.2\,\mathrm{fm}$, we find $E_B{\simeq}3.3\frac{\alpha_s}{r}$ or $E_B{\simeq}5\frac{1}{m_b r^2}$ for the two options above. Using $r(\Upsilon(2S)){\simeq}0.5\,\mathrm{fm}$ then gives $E_B(2S){\simeq}3.3\frac{\alpha_s}{r}{\simeq}0.4\,\mathrm{GeV}$ or $E_B(2S){\simeq}5\frac{1}{m_b r^2}\,{\simeq}0.16\,\mathrm{GeV}$. Since the first replacement is closer to the empirical $\Upsilon(2S)$ binding of $\sim$0.54 GeV, we will adopt it in our calculations.

Appendix B: Feeddowns and pp baseline cross sections for excited states

In this appendix we detail our implementation for updated feeddown fractions. Starting from Ref. [83], the direct $\Upsilon(1S)$ cross section is 70 %(50 %) at low (high) p_T, on average 67 %. The feeddowns to the $1S$ state are approximately 17 % from $1P$, 9 % from $2S$, 1 % from $3S$ and 6 % from $2P$ and $3S$ together. The main change from the previous work of Ref. [28] is from the $\chi_b(nP)$ states which now contribute less at low p_T [53]; cf. Table. I. Because of the newly included explicit treatment of the $\Upsilon(3S)$ state, we implement detailed feeddown fractions discussed below for the TBS calculation. For the SBS calculation, we only include $\Upsilon(1S)$, $\Upsilon(2S)$ and $\chi_b(1P)$ states. A correction from explicitly including $\Upsilon(3S)$ and $\chi_b(2P)$ states in the SBS calculation would result in ca. $\sim$10 % more regeneration for the $\Upsilon(2S)$ and a negligible contribution to the $\Upsilon(1S)$.

From several experimental data [58, 69–72, 84, 85], we conclude $\sigma_{2S} \simeq 0.33\sigma_{1S}^{\mathrm{tot}}$ and $\sigma_{3S} \simeq 0.15\sigma_{1S}^{\mathrm{tot}}$. With the branching ratios $Br(2S \to 1S) = 26.7\,\%$ and $Br(3S \to 1S) = 6.6\,\%$, we obtain feeddown fractions of $Fd(2S \to 1S){=}0.33 \cdot 26.7\,\% = 8.8\,\%$ and $Fd(3S \to 1S){=}0.15 \cdot 6.6\,\% = 0.99\,\%$, which are consistent with Ref. [83].

The cross section ratio of $\frac{\sigma(\chi_{b2}(1P))}{\sigma(\chi_{b1}(1P))} = 0.85$ from Ref. [86] indicates a smaller production of the heavier $1P$ state. An assumption for the lighter $\chi_{b0}(1P)$ with a ratio $\frac{\sigma(\chi_{b0}(1P))}{\sigma(\chi_{b1}(1P))} \simeq 1.5$ gives an approximate branching ratio for the $1P$ state of

$$\begin{aligned} Br(1P \to 1S) \;&\simeq\; \frac{Br(\chi_{b0}(1P) \to 1S)\cdot 1.5}{3.35} \\ &\quad + \frac{Br(\chi_{b1}(1P) \to 1S)\cdot 1.0}{3.35} \\ &\quad + \frac{Br(\chi_{b2}(1P) \to 1S)\cdot 0.85}{3.35} \\ &= \frac{1.8\cdot 1.5 + 33.9\cdot 1.0 + 19.1\cdot 0.85}{3.35}\,\% \\ &= 15.8\,\%\,. \end{aligned} \tag{B1}$$

We estimate a $1P$ cross section of $\frac{17\,\%}{15.8\,\%} \simeq 1.08$ of the inclusive $1S$ cross section, $\sigma_{1P} \simeq 1.08\sigma_{1S}^{tot}$. We estimate the fraction $\frac{\sigma_{2P}}{\sigma_{1P}} \simeq 0.8$ from Ref. [87] so that $\sigma_{2P} \simeq 0.864\sigma_{1S}^{tot}$.

Assuming the same ratio between different χ_b states for the $2P$ multiplet, we estimate

$$\begin{aligned} Br(2P \to 1S) \;&\simeq\; \frac{Br(\chi_{b0}(2P) \to 1S)\cdot 1.5}{3.35} \\ &\quad + \frac{Br(\chi_{b1}(2P) \to 1S)\cdot 1.0}{3.35} \\ &\quad + \frac{Br(\chi_{b2}(2P) \to 1S)\cdot 0.85}{3.35} \\ &= \frac{0.9\cdot 1.5 + 10.8\cdot 1.0 + 8.1\cdot 0.85}{3.35}\,\% \\ &= 5.7\,\%. \end{aligned} \tag{B2}$$

and

$$\begin{aligned} Br(2P \to 2S) &\simeq \frac{Br(\chi_{b0}(2P) \to 2S) \cdot 1.5}{3.35} \\ &+ \frac{Br(\chi_{b1}(2P) \to 2S) \cdot 1.0}{3.35} \\ &+ \frac{Br(\chi_{b2}(2P) \to 2S) \cdot 0.85}{3.35} \\ &= \frac{4.6 \cdot 1.5 + 19.9 \cdot 1.0 + 10.6 \cdot 0.85}{3.35}\,\% \\ &= 10.7\,\% \,. \end{aligned} \tag{B3}$$

The latter is almost the same as $Br(3S \to 2S) = 10.6\,\%$. These estimates result in feeddown fractions

$$\begin{aligned} Fd(2P \to 1S) &= \frac{\sigma_{2P} Br(2P \to 1S)}{\sigma_{1S}^{tot}} = 0.864 \cdot 5.7\,\% \\ &= 4.9\,\% \end{aligned} \tag{B4}$$

and

$$\begin{aligned} Fd(2P \to 2S) &= \frac{\sigma_{2P} Br(2P \to 2S)}{\sigma_{2S}} = \frac{0.864 \cdot 10.7\,\%}{0.33} \\ &= 28\,\% \,, \end{aligned} \tag{B5}$$

consistent with Ref. [83].

The above estimate furthermore leads to a total cross section for the higher excited $3S$ and $2P$ states of about $1.014\sigma_{1S}^{\rm tot}$. With $Br(3S \to 1S) = 6.6\,\%$ and $Br(2P \to 1S) = 5.7$, we have

$$\begin{aligned} &Fd(3S + 2P \to 1S) \\ &\quad = \frac{\sigma_{3S} Br(3S \to 1S) + \sigma_{2P} Br(2P \to 1S)}{\sigma_{1S}^{tot}} \\ &\quad = 0.15 \cdot 6.6\,\% + 0.864 \cdot 5.7\,\% = 5.9\,\% \end{aligned} \tag{B6}$$

and, with $Br(3S \to 2S) = 10.6\,\%$ and $Br(2P \to 2S) = 10.7$,

$$\begin{aligned} &Fd(3S + 2P \to 2S) \\ &\quad = \frac{\sigma_{3S} Br(3S \to 2S) + \sigma_{2P} Br(2P \to 2S)}{\sigma_{2S}} \\ &\quad = \frac{0.15 \cdot 10.6\,\% + 0.864 \cdot 10.7\,\%}{0.33} = 33\,\% \,, \end{aligned} \tag{B7}$$

consistent with Ref. [83].

Since the branching ratios from $3S$ or $2S$ to $1P$ are all smaller than 1 %, we neglect these feeddown channels.

[1] R. Rapp, D. Blaschke and P. Crochet, Prog. Part. Nucl. Phys. **65**, 209 (2010).
[2] P. Braun-Munzinger and J. Stachel, Landolt-Börnstein **23**, 424 (2010); [arXiv:0901.2500 [nucl-th]].
[3] L. Kluberg and H. Satz, Landolt-Börnstein **23**, 372 (2010); [arXiv:0901.3831 [hep-ph]].
[4] A. Mocsy, P. Petreczky and M. Strickland, Int. J. Mod. Phys. A **28**, 1340012 (2013).
[5] R. Rapp and X. Du, Nucl. Phys. A **967**, 216 (2017)
[6] E. Scomparin, Nucl. Phys. A **967**, 208 (2017)
[7] L. Ramello *et al.* [NA50 Collaboration], Nucl. Phys. A **715**, 243 (2003).
[8] A. Adare *et al.* [PHENIX Collaboration], Phys. Rev. Lett. **98**, 232301 (2007).
[9] L. Adamczyk *et al.* [STAR Collaboration], arXiv:1607.07517 [hep-ex].
[10] B. B. Abelev *et al.* [ALICE Collaboration], Phys. Lett. B **734**, 314 (2014).
[11] L. Grandchamp, R. Rapp and G. E. Brown, Phys. Rev. Lett. **92**, 212301 (2004).
[12] A. Andronic, P. Braun-Munzinger, K. Redlich and J. Stachel, Nucl. Phys. A **789**, 334 (2007).
[13] X. Zhao and R. Rapp, Phys. Rev. C **82**, 064905 (2010).
[14] Y. p. Liu, Z. Qu, N. Xu and P. f. Zhuang, Phys. Lett. B **678**, 72 (2009).
[15] X. Zhao and R. Rapp, Nucl. Phys. A **859**, 114 (2011).
[16] T. Song, K. C. Han and C. M. Ko, Phys. Rev. C **84**, 034907 (2011).
[17] E. G. Ferreiro, Phys. Lett. B **731**, 57 (2014).
[18] K. Zhou, N. Xu, Z. Xu and P. Zhuang, Phys. Rev. C **89**, 054911 (2014).
[19] S. Chatrchyan et al. [CMS Collaboration], Phys. Rev. Lett. **109**, 222301 (2012).
[20] L. Adamczyk *et al.* [STAR Collaboration], Phys. Lett. B **735**, 127 (2014).
[21] A. Adare *et al.* [PHENIX Collaboration], Phys. Rev. C **91**, no. 2, 024913 (2015).
[22] L. Adamczyk *et al.* [STAR Collaboration], Phys. Rev. C **94**, no. 6, 064904 (2016).
[23] B. Krouppa, R. Ryblewski and M. Strickland, Phys. Rev. C **92**, 061901 (2015).
[24] B. Krouppa and M. Strickland, Universe **2**, no. 3, 16 (2016).
[25] J. Hoelck, F. Nendzig and G. Wolschin, Phys. Rev. C **95**, no. 2, 024905 (2017).
[26] B. B. Abelev *et al.* [ALICE Collaboration], Phys. Lett. B **738**, 361 (2014).
[27] L. Grandchamp, S. Lumpkins, D. Sun, H. van Hees, R. Rapp, Phys. Rev. C **73**, 064906 (2006).
[28] A. Emerick, X. Zhao and R. Rapp, Eur. Phys. J. A **48**, 72 (2012).
[29] F. Riek and R. Rapp, Phys. Rev. C **82**, 035201 (2010).
[30] K. Zhou, N. Xu and P. Zhuang, Nucl. Phys. A **931**, 654 (2014).
[31] V. Khachatryan *et al.* [CMS Collaboration], Phys. Lett. B **770**, 357 (2017).
[32] M. He, R. J. Fries and R. Rapp, Phys. Rev. C **85**, 044911 (2012).
[33] M. He, R. J. Fries and R. Rapp, Phys. Lett. B **735**, 445 (2014).
[34] X. Du and R. Rapp, Nucl. Phys. A **943**, 147 (2015).
[35] L. Grandchamp and R. Rapp, Phys. Lett. B **523**, 60 (2001).
[36] N. Brambilla, J. Ghiglieri, A. Vairo and P. Petreczky, Phys. Rev. D **78**, 014017 (2008).
[37] F. Karsch, M. T. Mehr and H. Satz, Z. Phys. C **37**, 617

(1988).
[38] S. Y. F. Liu and R. Rapp, Nucl. Phys. A **941**, 179 (2015).
[39] M.E. Peskin, Nucl. Phys. **B156**, 365 (1979);
G. Bhanot and M.E. Peskin, Nucl. Phys. **B156**, 391 (1979).
[40] Y. Park, K. I. Kim, T. Song, S. H. Lee and C. Y. Wong, Phys. Rev. C **76**, 044907 (2007).
[41] M. Laine, O. Philipsen, P. Romatschke and M. Tassler, JHEP **0703**, 054 (2007).
[42] S. Hamieh, K. Redlich and A. Tounsi, Phys. Lett. B **486**, 61 (2000).
[43] S. Mukherjee, P. Petreczky and S. Sharma, Phys. Rev. D **93**, no. 1, 014502 (2016).
[44] L. Grandchamp and R. Rapp, Nucl. Phys. **A709**, 415 (2002).
[45] T. Song, K. C. Han and C. M. Ko, Phys. Rev. C **85**, 054905 (2012).
[46] X. Zhao and R. Rapp, Phys. Lett. B **664**, 253 (2008).
[47] J. P. Blaizot and J. Y. Ollitrault, Phys. Rev. D **39**, 232 (1989).
[48] F. Karsch and R. Petronzio, Z. Phys. C **37**, 627 (1988).
[49] S. Gavin and R. Vogt, Nucl. Phys. B **345**, 104 (1990).
[50] L. Gerland, L. Frankfurt, M. Strikman and H. Stöcker, Phys. Rev. C **69**, 014904 (2004).
[51] V. Greco, C. M. Ko and P. Levai, Phys. Rev. C **68**, 034904 (2003).
[52] X. N. Wang and F. Yuan, Phys. Lett. B **540**, 62 (2002).
[53] R. Aaij *et al.* [LHCb Collaboration], Eur. Phys. J. C **74**, no. 10, 3092 (2014).
[54] Z. Ye [STAR Collaboration], Nucl. Phys. A **967**, 600 (2017).
[55] A. Adare *et al.* [PHENIX Collaboration], Phys. Rev. C **96**, no. 2, 024907 (2017).
[56] M. Cacciari, S. Frixione, N. Houdeau, M. L. Mangano, P. Nason and G. Ridolfi, JHEP **1210**, 137 (2012).
[57] B. B. Abelev *et al.* [ALICE Collaboration], Eur. Phys. J. C **74**, no. 8, 2974 (2014).
[58] S. Chatrchyan *et al.* [CMS Collaboration], Phys. Lett. B **727**, 101 (2013).
[59] C. Flores, [CMS Collaboration] talk at Quark Matter 2017.
[60] CMS Collaboration [CMS Collaboration], CERN Report No. CMS-PAS-HIN-16-023.
[61] K. J. Eskola, H. Paukkunen and C. A. Salgado, JHEP **0904**, 065 (2009).
[62] The ATLAS collaboration, CERN Report No. ATLAS-CONF-2015-050.
[63] R. Aaij *et al.* [LHCb Collaboration], JHEP **1407**, 094 (2014).
[64] B. B. Abelev *et al.* [ALICE Collaboration], Phys. Lett. B **740**, 105 (2015).
[65] X. Du, M. He and R. Rapp, Nucl. Phys. A **967**, 904 (2017)
[66] H. van Hees, M. Mannarelli, V. Greco and R. Rapp, Phys. Rev. Lett. **100**, 192301 (2008).
[67] F. Prino and R. Rapp, J. Phys. G **43**, 093002 (2016).
[68] D. Acosta *et al.* [CDF Collaboration], Phys. Rev. Lett. **88**, 161802 (2002).
[69] G. Aad *et al.* [ATLAS Collaboration], Phys. Rev. D **87**, no. 5, 052004 (2013).
[70] V. Khachatryan *et al.* [CMS Collaboration], Phys. Rev. D **83**, 112004 (2011).
[71] R. Aaij *et al.* [LHCb Collaboration], Eur. Phys. J. C **72**, 2025 (2012).
[72] R. Aaij *et al.* [LHCb Collaboration], Eur. Phys. J. C **74**, no. 4, 2835 (2014).
[73] H. Niemi, K. J. Eskola, R. Paatelainen and K. Tuominen, Phys. Rev. C **93**, no. 1, 014912 (2016).
[74] E. Abbas *et al.* [ALICE Collaboration], Phys. Lett. B **726**, 610 (2013).
[75] G. G. Fronzé, arXiv:1612.06691 [hep-ex].
[76] I. Das, A. Lardeux, [ALICE Collaboration] talk at Quark Matter 2017.
[77] A. M. Sirunyan *et al.* [CMS Collaboration], CMS-PAS-HIN-16-008 and arXiv:1706.05984 [hep-ex].
[78] S. Chatrchyan *et al.* [CMS Collaboration], JHEP **1404**, 103 (2014).
[79] J. P. Blaizot, D. De Boni, P. Faccioli and G. Garberoglio, Nucl. Phys. A **946**, 49 (2016).
[80] R. Katz and P. B. Gossiaux, Annals Phys. **368**, 267 (2016).
[81] N. Brambilla, M. A. Escobedo, J. Soto and A. Vairo, Phys. Rev. D **96**, no. 3, 034021 (2017).
[82] S. Kajimoto, Y. Akamatsu, M. Asakawa and A. Rothkopf, arXiv:1705.03365 [nucl-th].
[83] A. Andronic *et al.*, Eur. Phys. J. C **76**, 107 (2016).
[84] J. Adam *et al.* [ALICE Collaboration], Eur. Phys. J. C **76** no.4, 184 (2016).
[85] R. Aaij *et al.* [LHCb Collaboration], JHEP **1306** 064 (2013).
[86] V. Khachatryan *et al.* [CMS Collaboration], Phys. Lett. B **743** 383 (2015).
[87] R. Vogt, Phys. Rev. C **81** 044903 (2010).